De-excitation dynamics of cold Rydberg atoms

Luca Asteria
ADVISOR: Dr. Oliver Morsch

Many-body physics aims at the deduction of the properties of large ensembles of interacting systems starting from the characteristics of the single components; these so-called emergent properties can not be easily deduced even in cases when the interaction between the elements of the ensemble has a simple form. In particular the large number of coupled degrees of freedom makes it difficult to predict the out-of-equilibrium dynamics of such systems, in particular there is a complete lack of analitycal solutions and simulations require a lot of resources [1]. In theoretical treatments, this problem is simplified with the aid of mean-field theories, which can have a limited range of applicability, or with numerical simulations on a restricted number of elements.

In this thesis we present experimental results on a many-body system composed of cold Rydberg atoms [7] in which the "simplification" of the dynamics is achieved by inducing a dissipative dynamics that leads to a simpler evolution of the system and allows us to obtain information on the original, more complex dynamics. We present a basic schematization of what we mean. Suppose that we have a system S, and an observable $x(S)$. Then if we perform measurements of x at different times, we can understand how $x(S(t))$ varies in time, which is only a fraction of the information contained in S. But if at the time t', we let the system evolve under the 'simple' dynamics condition, we could get more information on the system at the time t'; maybe we could also be able to access the observables $y(S(t'))$ and $z(S(t'))$, and, iterating the procedure for different values of t', we can get a deeper insight into the 'complex' dynamics.

We apply this concept to the dynamics of cold Rydberg atoms in cold clouds, where the van der Waals interaction causes the laser-driven dynamics of the internal and external degrees of freedom of the atoms to be correlated and thus forming a complex many-body system [13, 19].

The simpler dynamics we induce is based on the de-excitation of Rydberg atoms through a coupling with a fast-decaying level: the dynamics that follows then concerns only the atoms that are in the Rydberg state and not all the atoms in the ground state, and has a simpler 'updating rule' because the possible transitions are only decay-like, while a resonant coupling with the ground state can cause both an excitation of a ground state atom and a de-excitation of an excited atom. We show that with this system it is possible to infer information about the distribution of the interaction energies between the excited atoms at a given point of the excitation dynamics. From the energy distribution, it is possible to draw conclusions about the spatial configuration of the excitations.

The original contribution of this thesis concerns the development of the experimental setup needed for realizing the de-excitation phase in the laboratory of the Pisa BEC group.

This technical improvement is related to the frequency switch that one of the laser of the Rydberg excitation is subject to, in order to become resonant with the de-excitation frequency. The technical part of this work extends beyond the technique needed for the de-excitation; a chapter of this thesis is dedicated to the characterization of various multi-frequency excitation techniques. Some applications of similar techniques have already been demonstrated in recent works, such as [15, 18].

The experimental results obtained with their use, applied to different aspects of the Rydberg excitation dynamics which are the dynamics on resonance and the dynamics out of resonance, are reported in the chapters 4 and 5.

Part of the work reported in chapter 4, the extension of the seed technique to a regime of high seed number, is part of a publication currently under review at Journal of Physics B (arxiv:1602.01257).

The last chapter is dedicated to the de-excitation as a method to gain information about the excitation dynamics.

So far, de-excitation from Rydberg states has been used in a few experiments [14]. The purpose of the present thesis is to show that it can give an insight into the interactions between Rydberg atoms in terms of the energy distribution that is correlated with the distribution in real space. We also provide indications that de-excitation could be also used in the controlled preparation of spatial arrangments of Rydberg excitations, an application very desirable for a new promising research field, that of quantum simulation [3].

The core of the thesis is structured as presented above, and follows the two introductory chapters on the general principles of Rydberg atoms physics and a description of the experimental apparatus used to investigate such phenomena.

Contents

List of Figures

Chapter 1

General properties of Rydberg atoms

1.1 General properties of Rydberg atoms

This theorical chapter has the purpose of introducing the reader to the aspects of the physics of Rydberg atoms that are going to be of importance over the course of this thesis. A more complete overview of the topic can be found in numerous reviews [7]. Rydberg atoms are atoms excited to levels with high principal quantum number $n > 20$, so more properly we should refer to these levels as 'Rydberg' and not to the atoms.

These states have properties, such as large polarizabilies and long lifetimes, that differ dramatically from those of low-lying levels. These properties are of interest because they make Rydberg atoms easily controllable and detectable but also because they make possible the realization with Rydberg atoms of strongly interacting systems.

We start recalling the spectrum of the hydrogen atom, that has energies that depend on the principal quantum number n:

$$E_n = -\frac{Ryd}{n^2}$$

Where Ryd is the Rydberg constant ($\sim 13.6eV$).

For high n the energy of the states of every atom can be well approximated by the hydrogen-like spectrum by changing the definition of the Rydberg constant and adding a correction, called quantum defect, that accounts for the presence of core electrons whose contribution to the energy is usually well approximated by a $\sim \frac{1}{r^4}$ potential (with r distance between the electron and the nucleus). The energy of a level then depends

also on the orbital angular momentum l and on the total angulat momentum j:

$$E_{n,j,l} = -\frac{Ryd'}{(n - \delta_{n,j,l})^2} \tag{1.1}$$

where $\delta_{n,j,l}$ is the quantum defect correction and Ryd' is the modified Rydberg constant that accounts for the different mass of the nucleus and for the charge of the Coulomb potential.

As n increases the quantum defect correction becomes smaller and it is usually neglected when determining the scaling laws for the properties of the Rydberg atoms.

It is known that the orbital radius scales as n^2: given that for the ground state the Bohr radius is on the order of $10^{-10}m$, for a Rydberg state with $n = 100$ it can even reach the micrometers scale, forming something we can call a giant quantum object.

This property can be used to demonstrate the others we are interested in. At first, we can estimate that also the order of magnitude of the typical dipole moment, being proportional to the matrix elements of $\mathbf{r}$, scales as n^2 and this origins a high sensitivity to electric fields, but also a strong dipole-dipole interaction.

The Rydberg atoms also have longer lifetimes than low-lying levels, that typically decay within $10 - 100ns$, up to hundreds of microseconds for states with $n > 50$, because of the small dipole matrix elements between Rydberg states and low-lying levels. Actually, since the biggest matrix elements are found between states with near energy, the typical decay in an environment at room temperature is induced by the part of the blackbody radiation in the microwave region, and not by spontaneous emission. Before reaching the ground state, an electron visits numerous Rydberg states. The scaling law for the lifetime is $\sim n^3$.

Rydberg atoms are easily ionized, since their binding energy is smaller; the classic ionization field scales as n^{-4}, therefore can be as low as tens of V/cm. This is useful for detecting them because Rydberg states can be easily field ionized and the resulting electrons and ions can be revealed by charge multiplication thechniques.

The most impressive dependence on n is certainly that of the van der Waals coefficient C_6, which determines the strength of the van der Waals interaction between two Rydberg atoms:

$$V_{int} = \frac{C_6}{|\mathbf{r}_1 - \mathbf{r}_2|^6} \qquad C_6 \sim n^{11}$$

In the following sections, we explain how this interaction arises.

1.2 van der Waals interactions

A simple two-atom model can show how the van der Waals interaction originates [2]. We have two atoms (1 and 2) at distance $\mathbf{R} = |\mathbf{R}|\mathbf{n}$, that can exist in two Rydberg levels $|\alpha\rangle$ and $|\beta\rangle$ of opposite parity. We also consider a dipole-dipole interaction of the form

$$H^{int} = \frac{\boldsymbol{\mu}_1 \cdot \boldsymbol{\mu}_2 - 3(\boldsymbol{\mu}_1 \cdot \mathbf{n})(\boldsymbol{\mu}_2 \cdot \mathbf{n})}{|\mathbf{R}|^3}$$

where $\boldsymbol{\mu}_i$ is the operator associated with the dipole moment $e\mathbf{r}_i$ ($\mathbf{r}_i$ is the operator distance between the Rydberg electron and the nucleus and e the electron charge). In the Hilbert space we are considering ($|\alpha\alpha\rangle$,$|\beta\beta\rangle$,$|\alpha\beta\rangle$ and $\beta\alpha\rangle$), H^{int} connects only the first two and the last two states, because $\boldsymbol{\mu}$ has vanishing matrix elements between states of the same parity. We consider the subspace spanned by $|\alpha\alpha\rangle = |0\rangle$ and $|\beta\beta\rangle = |1\rangle$. We evaluate the off-diagonal matrix elements of H^{int} substituting $\boldsymbol{\mu}_{\alpha\beta}$ where due and since they depend only on $\mathbf{R}$ we can simply write them as $\frac{C_3}{|\mathbf{R}|^3}$ where C_3 is a constant that can be taken real. The total Hamiltonian can be written then in the form

$$H = \begin{pmatrix} 0 & \frac{C_3}{|\mathbf{R}|^3} \\ \frac{C_3}{|\mathbf{R}|^3} & \Delta \end{pmatrix}$$

with Δ the energy difference between the unperturbed states, that we suppose positive for convenience in a second passage. Diagonalization yields the new Eigenvalues:

$$E_\pm = \tfrac{1}{2}(\Delta \pm \sqrt{\Delta^2 + 4\frac{C_3^2}{|\mathbf{R}|^6}}).$$

We define now $R_{vdW} = \left(\frac{C_3^2}{\delta}\right)^{\frac{1}{6}}$.

If $\mathbf{R} \ll R_{vdW}$ the eigenvalues become:

$$E_\pm = \pm\frac{C_3}{|\mathbf{R}|^3}$$

whith eigenvectors $|\pm\rangle = \frac{1}{\sqrt{2}}(|0\rangle \pm |1\rangle)$.
In the opposite case, $\mathbf{R} \gg R_{vdW}$, we can see the wavefunction undergoes only a small change because the off-diagonal term has a smaller relative weight while the energy shifts by

$$E_1' - E_1 = -\frac{C_6}{\Delta|\mathbf{R}|^6},\ E_2' - E_2 = +\frac{C_6}{\Delta|\mathbf{R}|^6}$$

Thus R_{vdW} is the crossover distance between a dipole-dipole interaction that behaves as $\sim |\mathbf{R}|^{-3}$ and a van der Waals interaction that behaves as $\sim |\mathbf{R}|^{-6}$. We have also shown that, depending on the chosen state (α or β), van der Waals interaction can be attractive or repulsive .

Now we define $C_6 = \frac{C_3^2}{\Delta}$. Since C_3 comes from a dipole-dipole interaction (which scales as $n^2 \cdot n^2$) and Δ scales as n^{-3} (if we use the energy difference between two near Rydberg levels) we have also demonstrated the n^{11} scaling of the C_6 coefficient.

Its actual computation for a given state requires the knowledge of a certain number of matrix elements between more than just two states as in the model above, but the basic idea remains the one we have just reported.

The C_6 value for the $70s$ state of ^{87}Rb, which is the Rydberg state used throught this thesis, is $2\pi \cdot 1.2 THz \mu m^6 \hbar$. A more useful mnemonic rule for obtaining the strength of the interaction is the scaling remembering that when $|\mathbf{R}| = 10.9\mu m$, $V_{int} = 2\pi 1 MHz$.

In the following sections we are going to present some of the peculiarities due to this interaction.

1.3 Coherent dynamics

By coherent dynamics we mean an evolution of the wavefunction, and consequently of the expectation values of the observables, described only by the Schrödinger equation. This evolution always describes a pure state contrarly to the case when decoherence due to interactions with the environment causes the wavefunction to end up in a mixed state. Most of the experiments in this thesis have been performed in the incoherent regime but it is useful to describe the basic principle of the coherent dynamics because it constitutes a reference for the incoherent dynamics and also because it allows a first display of the behaviour of van der Waals interacting systems. We start recalling briefly the derivation of the Rabi oscillations for a two-level system coupled with a resonant light field, and we extend this treatment to the case when many two-level systems are coupled via a van der Waals interaction.

We start with the single-atom Hamiltonian, which is

$$H = |1\rangle\langle 1|\omega + (\frac{\Omega}{2} e^{-i\omega t}|0\rangle\langle 1| + h.c.) \tag{1.2}$$

where ω is the energy separation between the two levels and the Rabi frequency Ω is the strength of the laser coupling. It is easier to solve the Schrödinger equation in the

rotating frame $|1'\rangle = e^{i\omega t}|1\rangle$, $|0'\rangle = |0\rangle$ which makes the interaction term non dependent on time. To account for this change of reference, the Hamiltonian becomes

$$H' = H - |1\rangle\langle 1|\omega = \frac{\Omega}{2}\sigma_x \tag{1.3}$$

The integration of the Schrödinger equation $i\partial_t = H'\psi$ yields

$$|\psi(t)\rangle = e^{-i\frac{\Omega}{2}\sigma_x t}|\psi(0)\rangle \tag{1.4}$$

with σ_x the Pauli matrix, that can be rewritten in the form:

$$|\psi(t)\rangle = (cos(-i\frac{\Omega}{2}t)I - i \cdot sin(\frac{\Omega}{2}t)\sigma_x)|\psi(0)\rangle \tag{1.5}$$

where I is the identical matrix. It can be shown then that the populations evolve with a frequency that is exactly the Rabi frequency Ω:

$$|\langle 1|\psi\rangle|^2 = |sin(\frac{\Omega}{2}t)|^2 = \frac{1}{2}(1 - cos(\Omega t)) \tag{1.6}$$

Now we add another atom near the first one. We suppose that $|1\rangle$ is a Rydberg level.

Since the $|11\rangle$ level is coupled by the laser light to the $|10\rangle$ and $|01\rangle$ off resonantly, and supposing $V_{int} \gg \Omega$, we remove it from our system.

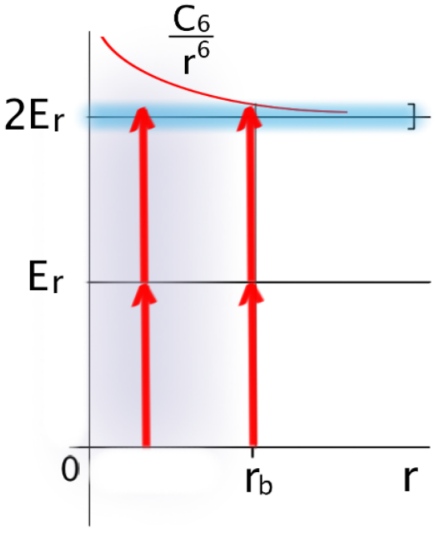

FIGURE 1.1: **Level shift due to inter-atom interaction.** Transitions towards the doubly-excited state from a single excitation state are shifted out of resonance if $V_{int} \gg \Omega$. V_{int} is represented by the red curve while Ω by the width of the blue contour.

Then in the rotating frame (the transform is performed as before on both atoms) the total Hamiltonian becomes:
$H = \begin{pmatrix} 0 & \Omega & \Omega \\ \Omega & 0 & 0 \\ \Omega & 0 & 0 \end{pmatrix}$ which, diagonalized, becomes $H = \begin{pmatrix} 0 & \sqrt{2}\Omega & 0 \\ \sqrt{2}\Omega & 0 & 0 \\ 0 & 0 & 0 \end{pmatrix}$
in the basis $|0\rangle$, $\frac{1}{\sqrt{2}}(|01\rangle + |10\rangle)$ and $\frac{1}{\sqrt{2}}(|01\rangle - |10\rangle)$. The ground state is coupled only to the entangled state $\frac{1}{\sqrt{2}}(|01\rangle + |10\rangle)$ with an enhanced collective Rabi frequency $\Omega_{coll} = \sqrt{2}\Omega$.

This can be generalized to a set of atoms that gives a collective Rabi frequency $\Omega_{coll} = \sqrt{N}\Omega$ between the ground state and a maximally entangled state where a single excitation is shared between all the atoms. Enhanced Rabi oscillations have been observed in [5, 4]. When we are examining excitation times longer than the laser coherence time, the picture changes. Infact laser decoherence causes loss of coherence between the ground state and the excited state with the result that the system 'decides' which atom is excited while the others remain in the ground state; this destroys the entanglement and the enhancement of the Rabi frequency. We describe in the next section the differences that arise in the fully incoherent regime which is the regime that characterizes the dynamics we are going to study experimentally.

1.4 Incoherent Dynamics and statistics

We describe briefly the theory for spins $\frac{1}{2}$ coupled with a $|\mathbf{R}|^{-6}$ potential, that can be found in detail in [9].

The Hamiltonian in the rotating frame is

$$H = \Sigma_k \frac{\delta}{2}\sigma_z^k + \frac{\Omega}{2}\sigma_x^k + \Sigma_{k,k'} V_{k,k'}$$

where δ is the detuning of the laser radiation from the atomic transition, Ω as before is the strength of the laser coupling and $V_{kk'}$ is a potential which is non-zero and has the van der Waals form only if both the atoms denoted by the indexes k and k' are excited to the Rydberg level. $\sigma_{x,y}$ are the Pauli matrices. We consider a source of decoherence that acts on the coherences between ground and Rydberg state of each atom with rate γ.

$$\partial_t \rho = i[\rho, H] + L\rho \tag{1.7}$$

with

$$L\rho = \gamma\Sigma_k (n_k \rho n_k - \frac{1}{2}(\{n_k, \rho\}))$$

The evolution for the matrix density can be simplified in the case where $\gamma \gg \Omega$. Basically in this regime coherences can be neglected and the matrix elements becomes diagonal, reducing the number of variables from $(2^n)^2$ to 2^n (with n number of atoms). The exact calculation that leads to the evolution of this reduced density matrix μ is fairly complex, so we show only the result and we comment it.

$$\partial_t \mu = \Sigma_k \Gamma_k (\sigma_x^k \mu \sigma_x^k - \mu) \tag{1.8}$$

where $\Gamma_k = \Gamma_0 (\frac{1}{1+(\frac{\delta - V_{int}}{\gamma})^2})$ and $V_k = \Sigma_{k'} n_{k'} (|\mathbf{r}_k - \mathbf{r}_{k'}|)^{-6}$
where n_k is the projection operator on the excited state. Since the rates Γ_k depend on V_k which in turns depends on the state of all the other atoms, they must be evaluated according to the configuration of the excitations.

What the master equation basically says is that each state (whose probability is a single diagonal entry of μ) has a channel of gain and a channel of loss with all the states that differ from it by a single flip ($\sigma_x^k \mu \sigma_x^k$), and the speed of the channel is governed by the rates Γ_k. The rate Γ_k contains information about the interactions because it has a lorentzian shape in function of the effective detuning which is the difference between the laser detuning δ and the interaction shift V_k.

The stationary solution is the tensorial product of identical density matrices for each atom, and therefore does not depend on the interactions.

What interactions change then is the path that the system follows to reach the stationary state i.e. the dynamics, and it is of much more interest than the steady state solution. Although the number of variables has been considerably reduced, solving the master equation analitycally is still an impossible task; the dynamics is usually simulated with a lower number of atoms than in a typical experiment and under some approximation which typically amount to neglecting the atomic motion and the disorder in the positions (usually regular positions on a lattice are used). In [9], we find also a numerical integration based on a mean field assumption. A dynamics described by such a master equation is no longer deterministic, because transitions are events which can occour with a certain probability. Typically in the experiment the observable which can be measured is the number of excitation; the associated quantity of interest then becomes the mean number of excitations, averaged over a sufficiently large amount of repetitions. Consequently we are interested in the amount of fluctuations from the mean value. We introduce the Mandel Q factor, or normalized second moment of the distribution [11]

$$Q = \frac{\langle \Delta N^2 \rangle}{\langle N \rangle} - 1 \tag{1.9}$$

which has the properties that: for a poissonian distribution, $Q = 0$, since $\langle \Delta N^2 \rangle = \langle N \rangle$.

For a subpoissonian distrubtion, i.e., one that has less fluctutations than a Poissonian of the same mean number we have $-1 < Q < 0$; and finally for a super-poissonain distribution (larger fluctuations than a poissonian one) the Q-parameter is larger than 0.

A deterministic process has $Q = -1$. The Q factor usefulness lies in the fact that a poissonian distribution is characterized by absence of correlation between the events that we are counting, therefore when $Q \neq 0$ we know that there is some sort of correlations that, in our case, are useful to study interactions. If a $Q \neq 0$ implies correlation, the other implication is not necessarely true: a correlated process can have $Q = 0$ too.

1.4.1 Dynamics on resonance

What happens when we point a laser resonant with the Rydberg transition on a sample of cold, ground state atoms? We can see from the definition of the rates Γ_k that in the ground state $\mu = |000..\rangle$ each atom has a rate equal to Γ_0, because both δ and V_{int} are zero. At a certain point, then, an atom will undergo a spin flip. What happens then is that the rate for the atoms that have $V_k > \gamma$, is strongly suppressed ($\Gamma \ll \Gamma_0$). This happens in a sphere centered around the first excitation of radius

$$R_b = \left(\frac{C_6}{\gamma} \right)^{\frac{1}{6}} \tag{1.10}$$

that is called blockade radius. This phenomenon, known as dipole blockade has been observed in a wide variety of contexts [13, 2].

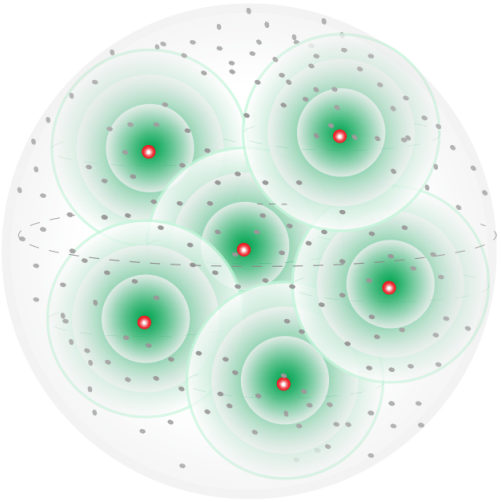

FIGURE 1.2: **Schematic representation of the excitation distribution in a blockaded dynamics** The presence of an excitation in a certain point decreases the probability of neighbours being excited; therefore the most likely configurations are the ones where the excitations are located at distances greater than R_b.

Then the second excitation will appear with much higher probability at a distance from the first greater than R_b; the third one will have accessible the total volume minus two blockade spheres and so on. When all the volume is filled with blockade spheres the resulting dynamics would evolve at a rate much slower than in the first part of the excitation.

In the experiment, when we study the number of excitations in function of the excitation time (we call such experiments time dependence) this slowing is clearly visible in form of a slope change of the curve.

What we expect on the Q factor is that the first part of the dynamics will be poissonian-like ($Q \sim 0$), because it is characterized by unrelated events and then gradually becomes sub-poissonian because there is an occurrence of the mean number which is highly likely and that number is about the ratio between the total volume and the volume of a blockade sphere.

1.4.2 Dynamics out of resonance

When the driving field, respect to the Rydberg transition has a detuning that has the same sign as the interactions, something really interesting happens. Now in the ground state $\mu = |000...\rangle$ the atoms can still be excited, only with a lower rate.

What happens when the first excitation appears, is that if the detuning has the same sign as the interactions they can produce again a rate which is the resonant one in

absence of interactions; this is true at a distance from the first excitation $r_{fac} = \left(\frac{C_6}{\delta}\right)^{\frac{1}{6}}$ called facilitation radius.

Since the rate has a lorentzian shape in function of the detuning we define a facilitation volume which is the shell of radius r_{fac} and width $\delta_r = \frac{1}{6} r_{fac} \frac{\gamma}{\delta}$ and it is the volume where the interactions make resonant the transition within a width given by the laser linewidth γ. If an excitation is created in the facilitation volume ('facilitated excitation') then a facilitation volume with a new shape appears (see fig. 1.3).

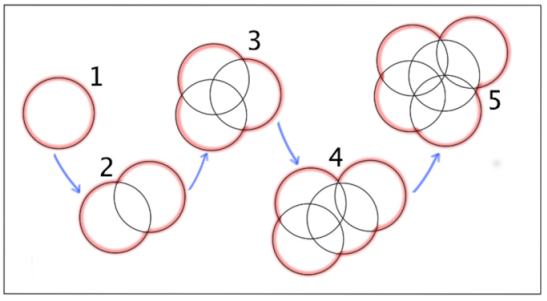

FIGURE 1.3: **Representation of a facilitated dynamics.** The presence of an excitation can lead to other excitations at a distance r_{fac} from the first; this facilitation can generate a highly correlated avalanche process

This feature is very notable, since the detuning of the driving implies a well defined length in the system; for example in a 1D system the presence of a first excitation would lead with high probability to the formation of a chain with spacing r_{fac}. The possibility of introducing a characteristic length in the system acting on the laser detuning is of great interest for experimental and theorical reasons, which vary from the creation of ordered systems, to the relation to Ising-like or lattice models. The first excitation that leads the facilitation process, can appear in a random time after the beginning of the experiment. The trigger of the facilitation process can be provided by a fast laser pulse on resonance which creates some Rydberg excitations in the first part of the experiment. This technique, which we are going to refer to as 'seed', was demonstrated in previous works [16] produced by the Pisa laboratory. The seed is an useful investigation instrument for the dynamics out of resonance, because it eliminates the degree of freedom of the starting point of the facilitation process which is a highly correlated process [10] . Noting that this simplification has been achieved with the use of two different frequencies in the same experiment (the resonant fast pulse and the remaining off-resonant pulse) we were motivated to extend the excitation schemes to other multi-frequency techniques other than the frequency switch which is required by both the seed and the de-excitation. We are going to present them in chapter 3.

Chapter 2

Experimental apparatus

A quick review of the experimental features is necessary in order to understand the system we are referring to when reporting our results; this helps providing a concrete representation of the phenomena we have introduced theoretically and also gives an idea of the possibilities and the limits characteristic of our investigation.

In particular, we focus on the elements which are more relevant for the work presented in the following chapters of the thesis. We start with a description of the magneto-optical trap (MOT), which is a laser light-based method that allows the creation of spatially confined cold ensembles of atoms (^{87}Rb in our case). This sample provides some optimal features for the Rydberg excitation, because of the reduced Doppler effect and the low scattering rate between atoms, both due to the low particle speed. Also, in the majority of experiments, the evolution of the external degrees of freedom happens in a timescale much longer than the evolution of the internal degrees of freedom of the atoms, therefore the atomic motion can be usually neglected (frozen gas approximation).

We explain then how the Rydberg excitation is performed in our experimental setup. Since the trapping of the atoms and the Rydberg excitation are not simultaneous but they alternate in a cycle, we explain how fast switching of the laser beams of the MOT and of the Rydberg excitation can be achieved.

This fast switching is performed with the aid of acousto-optical modulators (AOMs); we are going to see in detail how they function because they are a key part of the technical work that has been done during this thesis and that is going to be presented in the next chapter.

The final phase of the cycle is the measurement: through a ionization of the atoms in the Rydberg state and a successive detection of the ions we are able to count the number of Rydberg atoms. A quick overview of this procedure allows to understand what is the

observable of our system, and how this influences the analysis of the data collected with such a system.

2.1 The magneto optical trap (MOT)

The Magneto-Optical Trap [12] is a technique based on laser light which allows the simultaneous cooling and trapping of neutral atoms, down to $\sim 200\mu K$ in a volume of about $(100\mu m)^3$ in a typical case in this thesys.

The physics behind this process is as follows: an atom which absorbs a photon and then emits another photon by spontaneous emission receives, in average, a momentum equal to that of the first photon because the spontaneous emission doesn't have a preferred direction. By altering the probability of absorption in order to maximize this probability if the photon and the atom are counter propagating the atom feels a slowing force (cooling); by making this force (also) space-dependent a confining potential is obtained (trapping).

We sketch how the MOT principle works in a simplified 1D configuration (figure 2.1). Let's consider an atom which has two levels correspondent to an optical transition that have respectively $F = 0$ and $F = 1$ (hyperfine angular momentum) that implies the possible values for the F projection on the z axis f of 0 for $|F = 0\rangle$ and 0,$\pm$1 for $|F = 1\rangle$

The 1 level decays to the $|0\rangle$ level with a fast ($\sim MHz$) rate (γ). The atom is irradiated with light red detuned with respect to the $0 \to 1$ transition in the $-x$ direction with a σ_- polarized light (which connects the $|F = 0, f = 0\rangle$ and the $|F = 1, f = -1\rangle$ states) and in the +x direction with a σ_+ polarized light (which connects the $|F = 0, f = 0\rangle$ and the $|F = 1, f = +1\rangle$ states). The $|F = 1, f = 0\rangle$ state is not coupled to any other state. If a ground state atom is travelling in the $+x$ ($-x$) direction it is more likely to absorb a photon travelling $-x$ ($+x$), because of the Doppler effect that brings its frequency closer to resonance $\delta\omega = kv$ (the frequency shift is equal to the product of the wavevector of the radiation and the velocity of the atom), then in the average this tends to slow the atom and the two counterpropagating beams act as a viscous medium; the minimum temperature reachable with this method is known as Doppler limit and is on the order of $KT \sim \hbar\gamma$.

Then we add a magnetic field of the form $B = -bx\hat{z}$: this lifts the degeneracy of the $|F = 1\rangle$ level and splits it into three levels according to the Zeeman formula $\Delta E = -g_L\mu_B f \cdot bx$ (where g_L is the Landè factor, μ_B is the Bohr magneton). Then the $f = 0$ level has everywhere the same energy (but remains uncoupled), while the $f = 1$ and

$f = -1$ levels follows B (and then x, because of the choice of the magnetic field) with two opposite behaviours.

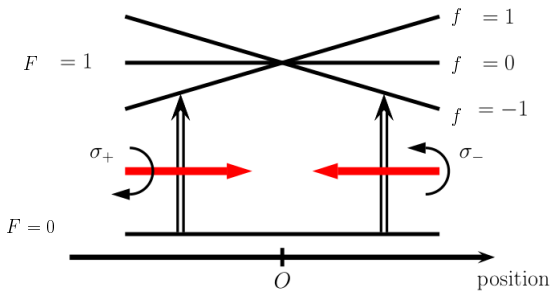

FIGURE 2.1: **Magneto-Optical Trap Scheme** Atoms are cooled and confined exploiting level shifts in a magnetic field gradient and absorption of photons with different polarizations

We can see that an atom on the right (left) will undergo mainly σ_- (σ_+) cycles because that transition is closer to resonance, therefore it will feel a force actrattive towards $x = 0$.

Putting togheter the two effects, the actual calculation, based on the stationary solution of the Bloch optical equations, yields a force which can be expanded in the first order in v and x:

$$F = -\alpha v - \beta x \tag{2.1}$$

where α is positive for a red detuning and β is proportional to b; this is valid when the Rabi frequency of each process Ω is lower than the decay rate γ.

Atomic levels can be more complex, in the case of Rubidium (figure. 2.2) and for the gradients of the magnetic field we use ($\sim G/cm$) we can treat the Zeeman splitting as a perturbation with respect to the hyperfine structure. The trap cycle is conducted between the $|5s_{\frac{1}{2}}, F = 2\rangle$ and $|5p_{\frac{3}{2}}, F = 3\rangle$ levels, which is a closed loop cycle because the $|5p_{\frac{3}{2}}, F = 3\rangle$ can decay only towards the $|5s_{\frac{1}{2}}, F = 2\rangle$ state because of the selection rule $\Delta F = 0, \pm 1$.

There is though a non-zero probability of exciting the $|5p_{\frac{3}{2}}, F = 2\rangle$ level which may decay in the $|5s_{\frac{1}{2}}, F = 1\rangle$ level which is no more coupled to the trap cycle, and atoms which end in this state would be lost from the trap. So we use another laser (called repump) which couples the $|5s_{\frac{1}{2}}, F = 1\rangle$ to the $|5p_{\frac{3}{2}}, F = 2\rangle$ that can again decay into the $|5s_{\frac{1}{2}}, F = 2\rangle$ starting again the cycle.

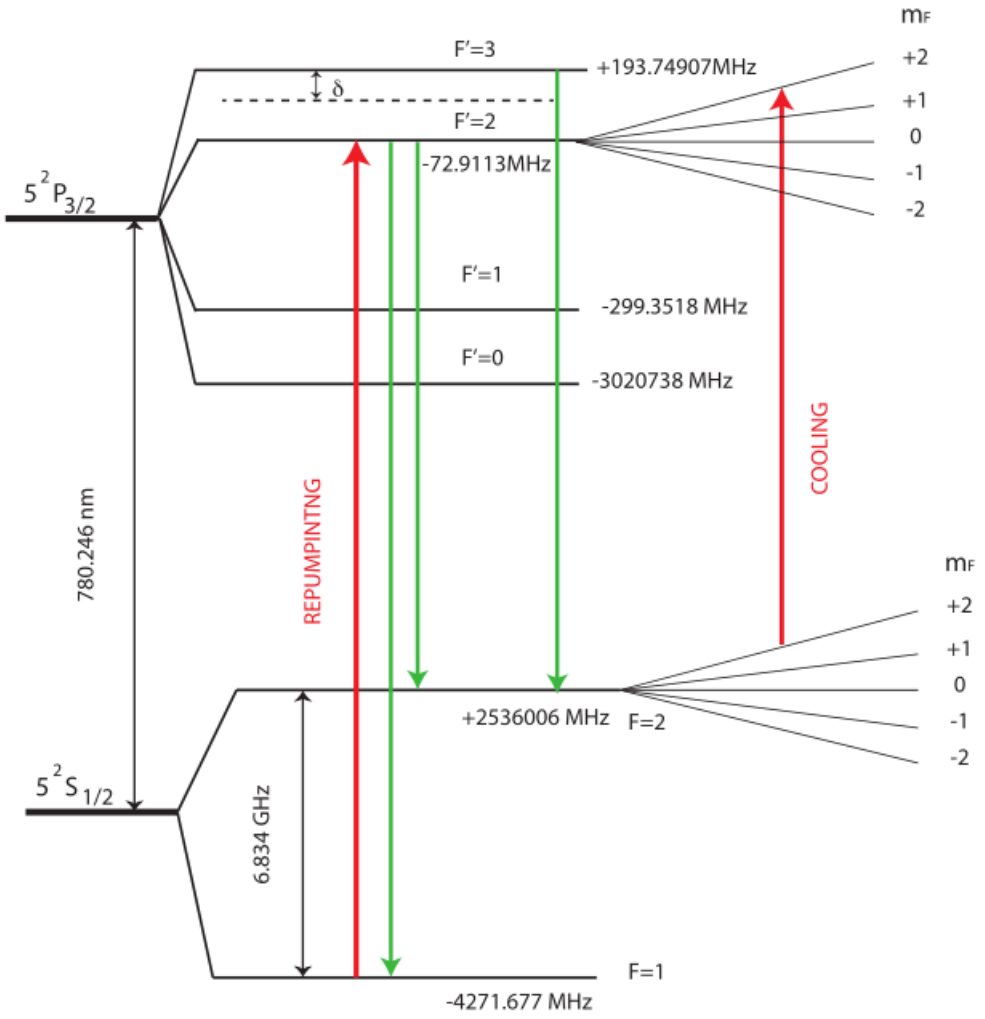

FIGURE 2.2: **^{87}Rb levels used in the MOT** The cooling and trappping cycle occurs between the states $|5s_{\frac{1}{2}}, F = 2\rangle$ and $|5p_{\frac{3}{2}}, F = 3\rangle$. The repump laser brings $|5s_{\frac{1}{2}}, F = 1\rangle$ atoms into the loop again. Laser transitions in red, spontaneous decay in green.

An actual MOT is composed by three pairs of counterpropagating beams with orthogonal polarizations and by three pairs of coils in anti-Helmotz configuration whose magnetic field vanishes in the middle point. The laser beams are focused in the same spot where the magnetic field has the zero value. This spot is contained in a vacuum chamber of pressure $10^{-10} mbar$ and it is the place where the cold cloud of atoms is located. The trap is recharged through a constant flux of atoms obtained by vaporization.

The magnetic field has a linear gradient for the spatial extension of the cloud. By adjusting the intensities of the currents of the coils this gradient can be changed and so the depth of the potential and the extension of the cloud. In our case, the temperature of the cloud is about $150\mu K$, while the dimensions of the gaussian shape range from $30\mu m$ to $200\mu m$. We deduce the form of the MOT with a CCD camera (with a resolution

of $3.3\mu m$) that detects the fluorescence of the trap cycle and through a software that can count the number of atoms with a 20% error that allows an estimation of the peak density; for our typical peak density ρ_0, which varies from 10^{10} to $10^{11} A/cm^3$ (number of atoms per cubic centimeter), we can consider the cloud a Boltzmann gas; from the temperature ($\sim 150\mu K$) we estimate a thermal velocity V_{TH} of $\sim 0.2\mu m\mu s$. The camera allows a measure of the density profile in two directions (x and y); we estimate the third one using $\sigma_z^2 = \sigma_x \sigma_y$.

The phase of trapping and the phase of Rydberg excitation happen in two distinct times; we control the timimg of both types of laser pulses using acousto-optical modulators (AOMs). In the next section we explain their mechanism since the technical work of this thesis, that we will report in the next chapter, concern the AOM of one of the lasers that are used for the Rydberg excitation.

2.2 The AOM

We focus here on the working of the AOM which is not only fundamental in the realization of the MOT, but also its understanding is crucial for the comprehension of the technical work which will be explained in chapter 3.

AOMs are used for fine and fast control of the laser frequencies, and for quickly turning on and off a light beam ($\sim 100ns$). They basically are crystals which are crossed by an acoustic wave, stimulated by the application of a voltage oscillating at a radio frequency (RF). The acoustic wave is absorbed by a particular material at the other end of the AOM and doesn't bounce back. When laser light hits an AOM, a photon-photon scattering with the absorption or stimulated emission of one phonon may happen (figure 2.3). In this case the outcoming photon's momentum and energy must satisfy:

$$k' = k_0 - k_{RF} \qquad \omega' = \omega_0 - \omega_{RF} \tag{2.2}$$

(in the case of emission of a phonon with wavevector k_{RF} and energy ω_{RF}, while in the case of absorption we use the plus sign). In analogy with Bragg's theory of diffraction from crystalline planes the condition on the wavevector will be referred to as Bragg condition and the scattered photon will be referred to as diffracted photon.
The RF and the light beam propagate in a orthogonal directions; this means that the Bragg condition influences the diffraction angle.

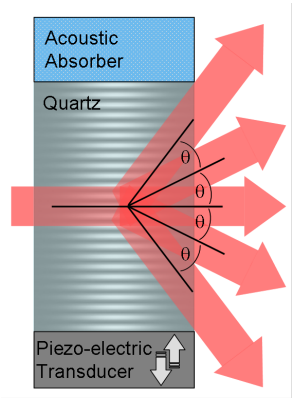

FIGURE 2.3: **Schematic representation of the AOM**. An acoustic wave travels from a piezo-electric material stimulated with a radio frequency towards the absorber. In the path, different numbers of phonon may be absorbed or emitted after a scattering with a photon than undergoes a change in its frequency and wavevector. Image Source: Wikipedia.org

Actually, scattering can involve two or more phonons and so the output of the AOM is composed by the unperturbed original beam or '0' order, the beam which corresponds to a one phonon absorption (emission) or +1 (-1) order, two photon absorption (emission), +2(-2) order and so on that are distinguishable because of the different angle. The Bragg condition can not be satisfied for all of them at once; and can be optimized only for one.

ω_{RF} is determined by an electronic device: this explains how its value can be controlled with precision and how the RF can be turned on and off fast. The time of reaction of the AOM is about the time that the acoustic wave needs to travel the waist of the laser. An AOM has a finite range of RFs that can generate an efficient diffraction; usually it is a range of about $\sim 40MHz$ centered around a central frequency of $50 - 150MHz$.

The control of the MOT beams with AOMs allows us to switch them on and off rapidly. They are switched off $5\mu s$ before the beginning of the experiment; in this case we are sure that the latter is performed from a state where all atoms are in the ground state, (given the decay time of the 5_p level which is $\sim 30ns$). The experiment begins when a RF is sent to the AOM of the lasers that generate the Rydberg pulse. After the desired time, this RF is switched off and, after $500\mu s$, the AOMs of the MOT beams are switched on again. During this dark period the atomic cloud begins to expand because of the finite temperature, when the MOT beams are switched on again they restart capturing the atoms. The whole cycle is repeated with a frequency of 4 Hz, which allows to take $\sim$ 200 repetition of an experiment in less than a minute. Than each experiment is composed by different 'shots' or experimental points which in turn are composed by a number of repetition which is usually ~ 100. The greater the number of repetition, the better the precision by which we determine the mean number and the Q factor of a

given process. Since the fluctuations of such measures is intrinsic in the behaviour of the system, the notion of error of measure on the experimental point can be misleading, and for this reason we do not report errors in our graphs. However, the value of the standard deviation of a process can be deduced by the Q factor when reported.

2.3 The excitation scheme

The Rydberg state used in the experiments reported in this thesis is the $|70s\rangle$ as we have mentioned;

it is reached by a two-photon process by mean of a 421nm laser, which couples the ground state $|5s\rangle$ with the intermediate level $|6p_{\frac{3}{2}}\rangle$, and a $1012nm$ laser, which couples the $|6p_{\frac{3}{2}}\rangle$ with the $|70s\rangle$. A detuning δ_{Blue} of about $400-600MHz$ of the first transition avoids the population of the intermediate state; the coupling between the ground state and the Rydberg state can be described by an effective Rabi frequency whose amplitude and frequency are given by:

$$\Omega_{Ryd} = \frac{\Omega_{421}\cdot\Omega_{1012}}{\delta_b} \qquad \omega_{Ryd} = \omega_{421} + \omega_{1012}$$

where ω_{421} and ω_{1012} are the frequencies of the two lasers and Ω_{421} and Ω_{1012} their Rabi frequency. The two-photon process is the only one (i.e. the intermediate state is not populated) as long as $\Omega_{Ryd} \ll \delta_{Blue}$.

The 421nm and 1012nm beams are switched on and off by use of AOMs too. The 421nm laser can be sent to the atoms directly or via an optical fiber. These two possible configurations are referred to as 3D and 1D respectively. The reason is that in the 3D configuration the 421nm and the 1012nm lasers are copropagating, thus creating an interaction volume with width of the order of the 421nm laser waist (which is about $40\mu m$, while the 1012nm laser has a larger waist of about $80\mu m$). Since the waist of the blue laser is greater than the blockade radius, we can have neighboring excitations along any direction. Instead in the 1D configuration the waist of the blue laser is only $\sim 6\mu m$, which is less than the blockade radius and a length comparable with a typical facilitation radius, therefore we expect that in this case excitations tend to dispose along the direction of the beam. Typically, the 1D configuration allows a simpler interpretation of the experiment while the 3D configuration can be used to magnify an effect because a wider possibility of interaction is presented.

2.4 Detection

We detect Rydberg atoms with a field ionization and then with a a charge multiplying device (a channeltron in our case). In order to be sure that we are detecting ions that come from field ionization, we wait $30\mu s$ after the process of excitation to ensure that residual ions which could have been formed by other processes (for example, population of the intermediate state of the two-photon process which is ionized by a second absorption of a $421nm$ photon) have moved away. This waiting time has been determined by a previous measurement.

After this waiting time, an electric field of $16V/cm$ ionizes the Rydberg atoms. The ions thus created are directed with another electric field towards the channeltron whose signal, recorded by an oscilloscope and analyzed by a software which contains a peak finding routine, allows the counting of the number of ions. Above a number of ions of about $30 - 40$ the resolution of the oscilloscope becomes comparable to the mean time interval between different ions so we perform measures with mean number under that limit. The whole detection has an efficiency (estimated) of about $\eta = 40 \pm 10\%$.

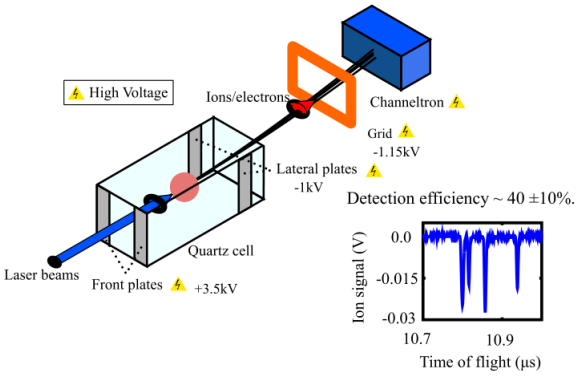

FIGURE 2.4: **Scheme of the detection procedure** An electric field ionize the Rydberg atoms and accelerates the ions towards the channeltron. Its signal (on the right) allows to count them one by one

This means that when we perform a series of measurements, the measured mean number will be $\eta\langle N_{real}\rangle$ and that also the statistics will be changed.

With some effort it is possible to demonstrate that also $Q_{observed} = \eta Q_{real}$ [17]. When we report an experimental value, we report the result of the measure and not its estimated real value.

This section about the detection of the Rydberg atoms closes the chapter about the experimental setup. At this point we have introduced all the elements necessary for the comprehension of the following chapters of the thesis, which consist of a technical

optimization of the apparatus we have just described, needed for the implementation of the de-excitation. This optimization has lead also to the characterization of more complex excitation techniques that are going to be described in the folllowing chapters. The results that these have produced are reported in chapters 4 and 5, while the last chapter is dedicated to the results of de-excitation.

Chapter 3

Multi-Frequency techniques

The implementation of the de-excitation phase in our experimental procedure has needed an optimization of the experimental setup: here we quickly explain the reason. A typical de-excitation experiment involves two parts: in the first one, some atoms are brought to the Rydberg state with the usual two-photon scheme ($421nm$ and $1012nm$), in the second one the $1012nm$ laser alone de-excites them. Since in the first part the $1012nm$ frequency must satisfy $\omega_{5s\rightarrow 70s} = \omega_{421nm} + \omega_{1012nm}$ and in the second one $\omega_{6p\rightarrow 70s} = \omega_{1012nm}$ this involves a frequency switch in the 1012 laser, performed by changing the RF that is sent to the AOM of the $1012nm$ laser.

This poses mainly two problems: the diffraction angle and the power of the output beam of the AOM depend on the RF. Ideally, instead, we would want $\Omega(r)$ not to be frequency dependent.

During this work of thesis the optical path of the $1012nm$ laser has been changed in order to include a double-pass into the AOM: this configuration, known as cat's eye, eliminates the angle problem, while the power problem is solved by a simple experimental procedure. Both are described in this chapter.

The cat's eye also allows a wide variety of multiple frequencies excitation techniques, which can involve a time-dependent frequency or the simultaneous use of different frequencies.

Research in this direction is motivated by the results of the 'seed' technique, based on the idea that a fast pulse on resonance with the Rydberg transition can be used to trigger the dynamics out of resonance, thus allowing the control of an event characterized by high fluctuations (see chapter 1).

Some of these multiple-frequencies protocols have been investigated during the thesis period:

- Among the techniques that make use of a time-dependent frequency we have considered discrete jumps and continuous sweeps.
- Among the techniques that use different simultaneous frequencies we have considered frequency modulation and line broadening.

in this chapter we review their technical aspects and implementations; typically this is a work of analysis of the electric signals followed by a check on the system. The results obtained with these techniques are presented in chapter 4 and 5 of this thesis.

3.1 Cat's eye

The cat's eye is a configuration of the optical path where there is a double pass of the beam in the AOM: the diffracted beam is reflected back and diffracted again. While the single pass diffraction implies a correlation between the exit angle and the RF, because of the Bragg condition, the double pass erases the memory of the two scatterings in the photon momentum, but gives a doubled frequency shift.
Here is how it works (figure 3.1):

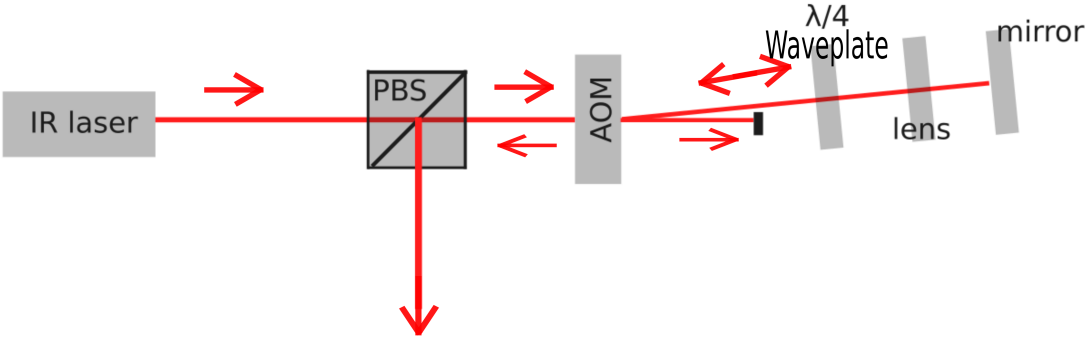

FIGURE 3.1: **Cat's eye scheme.** The output photon exits with the same angle for each radio frequency because the Bragg condition in the second diffraction forces it to come back exactly on its own incoming path

Laser light, with the polarization that allows transmission through the polarizing beamsplitter, is focused on the AOM. A convex lens, at a distance from the AOM equal to its focal length, and a mirror act like a spherical mirror with the center at the AOM position, reflecting each ray on its incoming path. Therefore, the exit angle for the second pass coincides with the initial input angle because of the unchanged Bragg condition. The use of a two-times crossed $\lambda_{\frac{\pi}{4}}$ waveplate rotates the polarization by $\frac{\pi}{2}$ allowing the

separation of the incoming beam and of the two-times diffracted beam, which is reflected from the beam splitter and sent towards the MOT. The orders of diffraction we are not interested in are mechanically stopped before the lens.
An equivalent way to see this process is based on the photon-phonon scattering picture: the first diffraction produces a change in the wavector of the photon $k = k_0 + k_{RF}$ (where k_{RF} is the phonon wavevector); the perpendicular incidence on the mirror gives a -1 factor producing $k = -k_0 - k_{RF}$ and the second diffraction cancels the dipendence on k_{RF} and therefore on the RF: $k = -k_0 - k_{RF} + k_{RF} = -k_0$
On each pass, the frequency changes by ω_{RF}, and in the end we have: $\omega = \omega_0 + 2\omega_{RF}$ (with ω_0 and ω initial and final photon frequency and ω_{RF} the phonon frequency). The doubled frequency shift is also a positive side-effect because it doubles the effective frequency range that can be used in experiments with variable frequency (it becomes $\sim 60MHz$, twice the bandwidth of the AOM).

On the other hand the efficiency $e = \frac{P_{out}}{P_{in}}$ depend more strongly on ω_{RF}: $e'(\omega_{RF}) = e(\omega_{RF})^2$ (figure 3.4).
In our setup we have used a convex lens of $10cm$ focal length at about 10cm from the AOM; the mirror is located about 20cm from it. We use the (-1) order (arbitrary choice): the scattered photon has less energy than the original one.
We verify that the cat's eye has reduced the displacement of the beam as a function of the RF. We use a beam-profiler, a CCD that allows to see in real time (via software) the shape of a pulse with a resolution of $1\mu m$. The beam-profiler is put at the MOT position in an equivalent optical path realized putting a mirror between the lens that focuses the $1012nm$ beam on the MOT and the vacuum chamber: the mirror is tilted in a way that reflects the beam towards the beam profiler which is put at a distance from the mirror equal to the distance between the mirror and the MOT. This method allows to see how much the light beam moves once it is sent to the MOT.

We can see (figure 3.2) that in the range $50MHz - 80MHz$ the cat's eye reduces the displacement from about $\sim 100\mu m$ to about $15\mu m$, while in the range $60Mhz - 80MHz$ we go from $\sim 100\mu m$ to $3\mu m$. Notice that the actual frequency changes two times faster than the RF, so there is a gain of another 2 factor in the ratio frequency/displacement.

Since the laser waist (the range over which $\Omega(r)$ changes significantly) is about $90\mu s$ we conclude that we can neglet the residual displacement.

In the sections that follow, we discuss the effect of the cat's eye on each technique, in particular the doubled frequency shift.

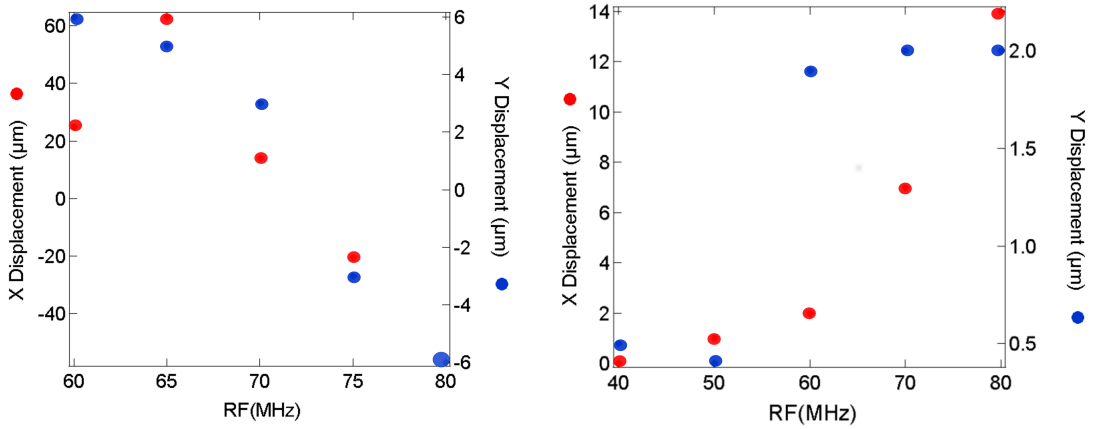

FIGURE 3.2: **Comparison of the beam displacement on the MOT position without (left) and with (right) the cat's eye.** Adding the cat's eye reduces the displacement due to the change of radio frequency to less than a beam waist ($90\mu m$).

3.2 Frequency jumps

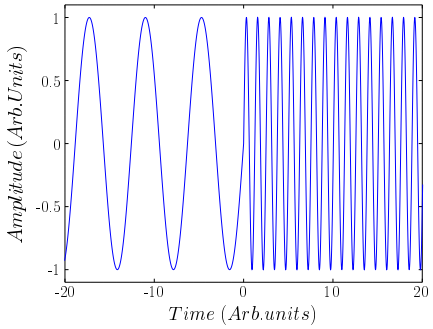

FIGURE 3.3: **Frequency Jump** At a certain point, the frequency changes value

This technique is the one used in the de-excitation experiment. The change in the $1012nm$ laser frequency is performed by means of an electronic switch which receives two RF signals as inputs and outputs only one of them according to the value of a control TTL signal. The switch between the two happens in a time of about $200 - 300ns$.

The use of two different RF sources has the advantage of making possibile the independent variation of each of them. On the other side, studying the response of the system to the variation of only one RF (of two) present a technical complication respect to the case where only one frequency is used. In the latter case in fact the frequency can be varied directly changing the lenght of the laser cavity, a process which doesn't alter Ω because it acts directly on the initial photon frequency ω_0.

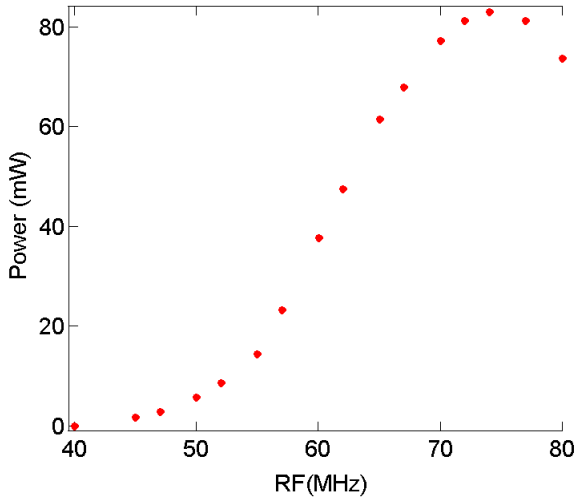

FIGURE 3.4: **Double pass transmission** Measurement of the optical power versus the applied radio frequency with fixed amplitude of the radio frequency.

When instead we want to vary the RF while keeping fixed the output optical power, the experiment must be preceded by a phase of calibration, that works as follows.

We first choose the desired output optical power, then for each of the RFs we are going to use, we find the amplitude of the electric signal the produces the desired optical power.

3.3 Sweeps

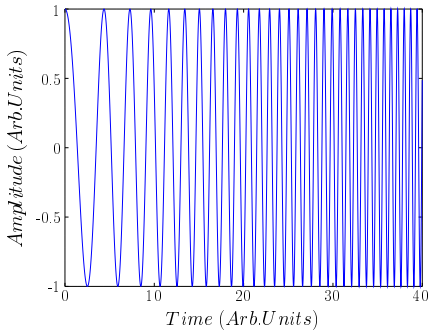

FIGURE 3.5: **Frequency sweep** The instantaneous frequency varies linearly in time

A 'sweep' is an excitation protocol where the instantaneous frequency is increased in time; we are interested in linear variations of the frequency $\omega(t) = \omega_0 + \frac{\Delta\omega}{\Delta t}t$ because the simplest situation offers an easier interpretation of the experimental results. In a certain sense a sweep is the continuous version of the frequency jump.

We implement it by means of a Voltage Controlled Oscillator (VCO), a chip that generates a RF according to a control voltage V.
In our case the relation between voltage and frequency is not easily predictable, because of the non-flat (in frequency) response of the chip. So we have to characterize different sweeps of the control voltage $V(t)$ studying the resulting sweep in frequency space $\omega(t)$. We measure the instantaneous frequency with FFT of the VCO signal on a temporal width of 200ns (~ 20 oscillations at $100MHz$). We then obtain the value of $\frac{\Delta\omega}{\Delta t}$ (slope of the frequency in function of time) with a linear fit in the linear zone.

The characterized sweeps have slopes which range from about $0.3MHz/\mu s$ to about $7MHz/\mu s$ in both negative and positive directions. The upper limit is given by the voltage source while the lower limit is dictated by the increasing importance of non-linearities (figure 3.6).

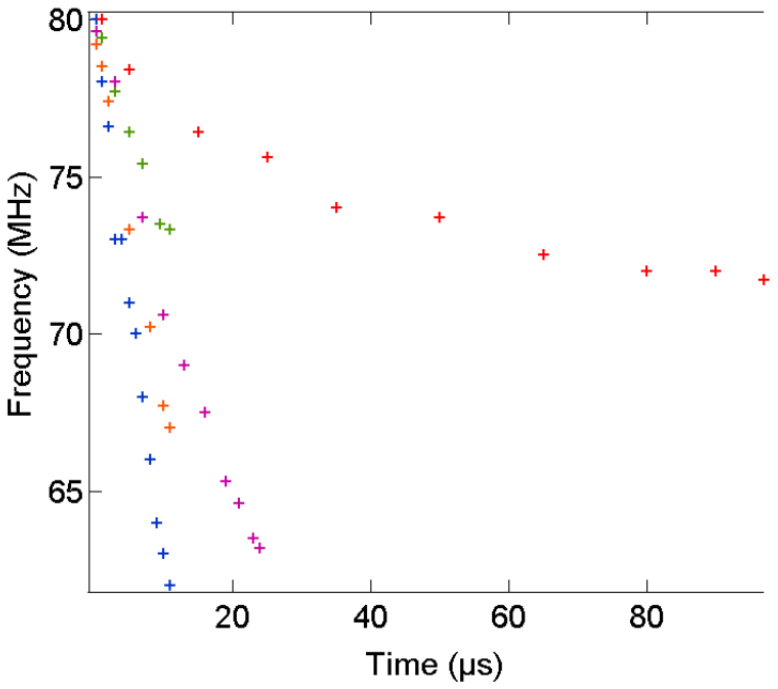

FIGURE 3.6: **Instantaneous frequency in function of the sweep time for different voltage sweeps** Red=$0.07V/\mu s$, green=$0.2V/\mu s$, purple=$0.28V/\mu s$, orange=$0.4V/\mu s$, blue=$0.56V/\mu s$. t_{max} for each sweep is determined by the time the control voltage needs to reach its maximum amplitude

We noted that the VCO instantaneous output amplitude decreases as the RF increases, and viceversa. Since this behaviour is the opposite to that of the AOM, we directly

measured the instantaneous optical power with a fast photo diode (Figure 3.7) finding that the two effects tend to compensate each other and the relative variation of power is less than $2-3\%$, a fraction we can neglet since we are not going to perform measurements of precision: for example, studying a process which has $\langle N \rangle = 10$ and $Q \sim 0$ the fluctuations are on the order of $\frac{\sqrt{10}}{10} \sim 30\%$.

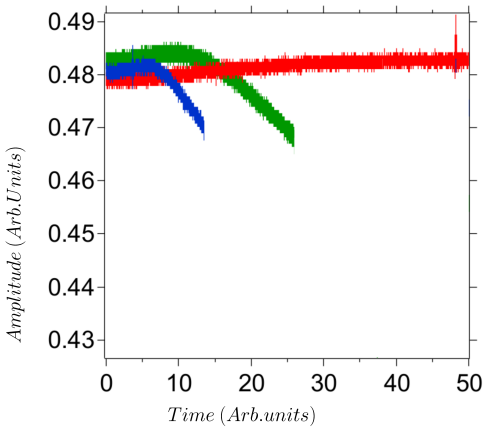

FIGURE 3.7: **Instantaneous output power for different frequency sweeps** red=$0.07V/\mu s$, green=$0.28V/\mu s$,blue=$0.56V/\mu s$.The frequency range that the RF scans from $t = 0$ to t_{max} is respectively $6MHz$,$20MHz$, $20MHz$. t_{max} for each sweep is determined by the time the control voltage needs to reach its maximum amplitude

The final test for each technique is to be done directly on the system in order to verify the response of the AOM.

We call 'frequency scan' an experiment where the frequency is varied in order to check a resonance or to measure a linewidth; we use it in this chapter in the specular way, as a method to use the system to probe the light. Infact these experiment are performed in a regime where the number of excited atoms is, to a certain approximation, proportional to the spectral intensity of light at the resonant frequency. When we send a composite spectrum to the AOM, there are multiple resonance conditions, one for each part of this spectrum. Then if we expect that the number of excitations in function of the frequency of the laser cavity is a specular reconstruction of the spectrum of the RF.

In the case of sweeps we verify that the atoms 'see' the expected frequency displacement performing frequency scans at different times of the voltage sweep (Figure 3.8). We select the time window of the sweep that corresponds to the desired frequency with a TTL switch between the RF source and the AOM. We can say that the AOM manages to follow the frequency sweep because the centers of the frequency scans shift with the expected velocity. When comparing results and expected values we have to consider a two factor because of the double pass in the AOM. Note also the fact that the center of the frequency scans shifts in the same direction of the sweep, because the resonance is

met at the condition $\omega_{Ryd} = \omega_0 - 2\omega_{RF}$; the minus sign due to the use of the -1 order of the AOM.

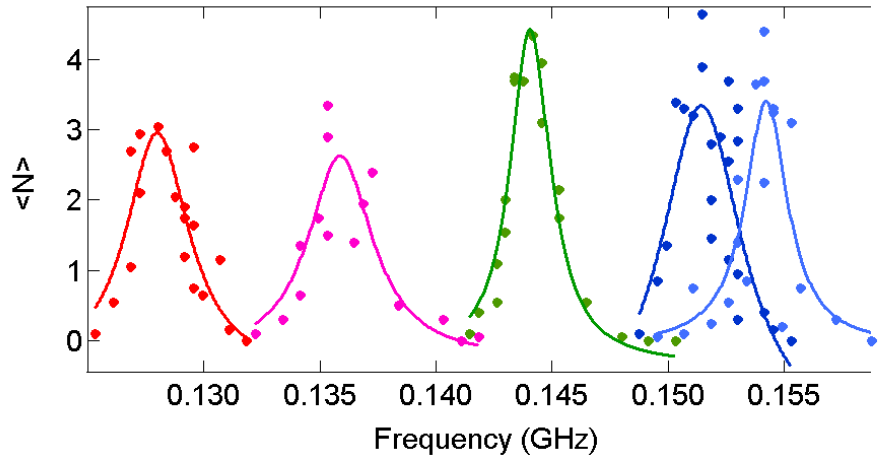

FIGURE 3.8: **Sweep test on the atoms** Frequency scans at times $0\mu s$ (red),$5\mu s$ (pink),$10\mu s$ (green),$15\mu s$ (blue),$18\mu s$ (light blue) after the start of a sweep with slope $0.75MHz/\mu s$. Excitation time of $1\mu s$. The resonance condition is met at a frequency that shifts with a slope which is 2 times the sweep slope beacuse of the double pass into the AOM.

In this thesis we have used only linear protocols but their workings demonstrate nevertheless that more sophisticated protocols can be studied, for example non-linear protocols or simultaneous variation of Ω [18].

3.4 Frequency modulation (FM)

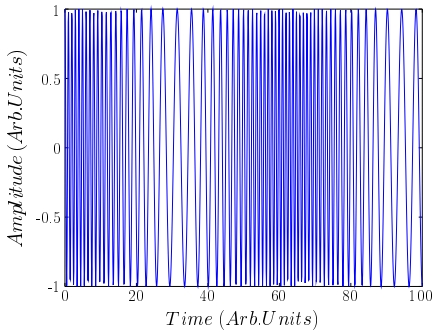

FIGURE 3.9: **Frequency Modulation** The instantaneous frequency is a sinusoidal function of time

Frequency modulation is a technique which offers a great control over the spectrum of a wave using only two control parameters, namely the frequency and the amplitude of a control voltage V; its main interesting feature is the possibility to increase the spectral width of the RF up to tens of MHz.

Here we recall the basic principles of Frequency Modulation, we explain how it can be applied to our system and the work of characterization that has been done in order to use it.
A wave is modulated in frequency when its instantaneous frequency is itself a sinusoidal function of time

$$\omega(t) = \omega_c + \omega_d sin(\omega_m t) \tag{3.1}$$

with ω_c the central frequency (called the carrier), ω_d modulation depth and ω_m modulation frequency. We obtain it just by sending a sinusoidal wave to the VCO input. Then we expect a dependence of ω_d from V (Voltage, also referred to as modulation amplitude).

Integrating the relation between phase and frequency $\partial_t \phi = \omega(t)$ the aspect of the wave is found:

$$w(t) = e^{i(\omega_c + \frac{\omega_d}{\omega_m} cos(\omega_m t))} = e^{i(\omega_c + n_m cos(\omega_m t))}$$

with $n_m = \frac{\omega_d}{\omega_m}$ index of modulation. The Fourier transform of such a wave is known:

$$\tilde{w}(\omega) = \Sigma_{k \in Z} i^k J_k(n_m) \delta(\omega_c + k\omega_m)$$

where J_k are the k^{th}order Bessel J functions and δ is Dirac's delta.
The spectrum is discrete, and has components (sidebands) which differ from ω_c (carrier) only by integer multiples of ω_m.

The intensity ($I(\omega) = \tilde{w}(\omega)^2$) of the k^{th} frequency is then proportional to J_k^2 and since $|J_k| = |J_{-k}|$ the spectrum is symmetric and centered around the central frequency ω_c

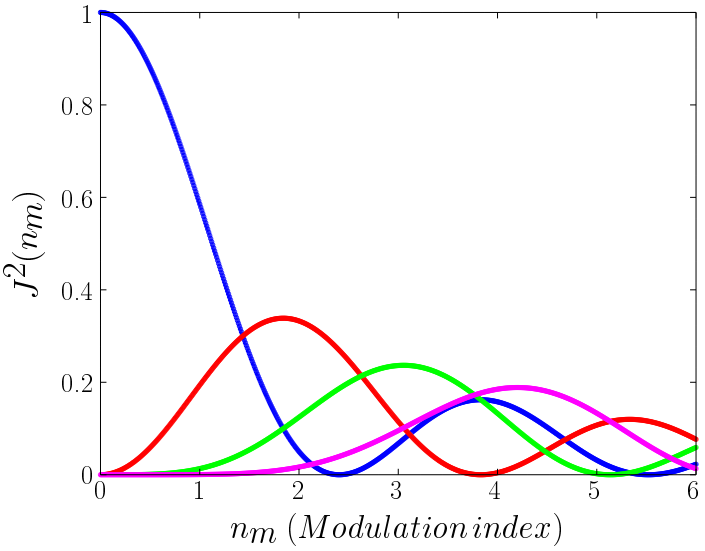

FIGURE 3.10: **Squares of the Bessel functions $\mathbf{J_k^2}$** $k = 0$ (blue), $k = 1$ (red), $k = 2$ (green), $k = 3$ (pink) versus modulation index. The higher the order, the higher the modulation index n_m of the first peak; this explains why increasing n_m the spectrum width increases.

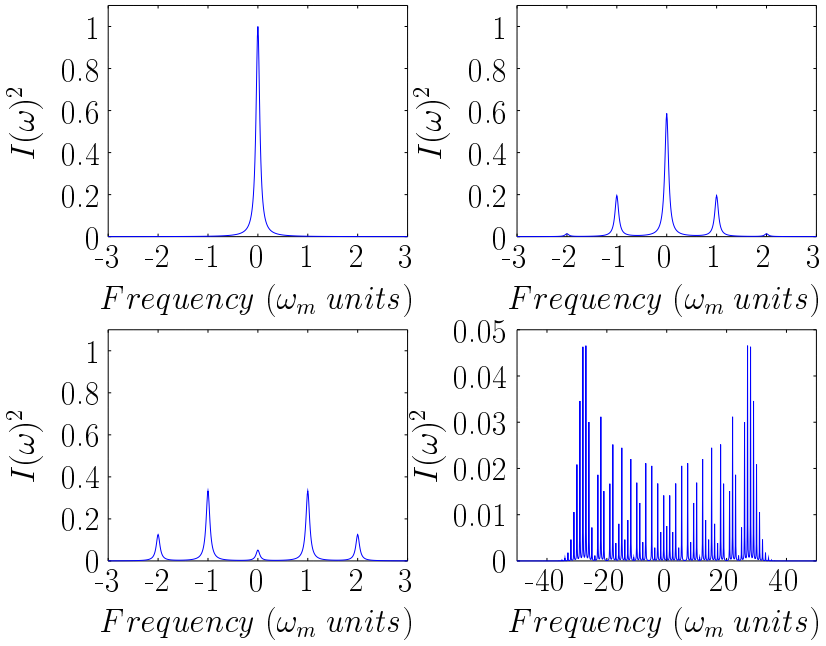

FIGURE 3.11: **Spectral Distribution for different $\mathbf{n}_m$**. Top: $n_m = 0$ (left); $n_m = 1$ (right). Bottom: $n_m = 2$ (left); $n_m = 30$ (right). The spectral width increases with n_m. The graph for $n_m = 30$ has different axis; linewidth is artificial and inserted for clarity.

Keeping in mind fig. 3.10 we can see how frequency modulation can be used to alter the spectrum width. $J_n(0) = \delta_{n0}$; infact in absence of modulation ($n_m = 0$) only the carrier

frequency is present (figure 3.11a). As we increase n_m other sidebands start to appear and the carrier's height decreases (figures 3.11b-3.11c); when $\omega_d \gg \omega_m$ the distribution is usually well approximated by a rectangle with half width equal to ω_d (figure 3.11d).

Since $\Sigma_{k\in Z} J_k^2(n_m) = 1$ Frequency modulation does not change the total power, which is spread over a larger range of frequencies.

We analyze with FFT the electrical signals, finding that they are well described by the ideal model which contains only the parameters n and ω_m (or ω_d and ω_m because only two of them can be independent variables) at least in the frequency range of interest.

The measure of n_m is performed as follows. When $n_m \gg 1$ the modulation depth ω_d can be estimated by measuring the half width of the spectrum (see fig. 3.11 for the $n_m = 30$ case). Otherwise we obtain the index of modulation n_m with an indirect method: at a given modulation amplitude we measure the ratio of the height of two different FFT peaks, which are proportional to the spectral intensity, and see what is the value of n_m which yields the same ratio between the corresoinding J_k^2. We discriminate between the infinite possibile solutions by turning off the modulation amplitude to zero and counting the number of zeros of a given sideband crossed. We found that in both regimes the modulation depth ω_d is proportional to the modulation amplitude (Figure 3.12).

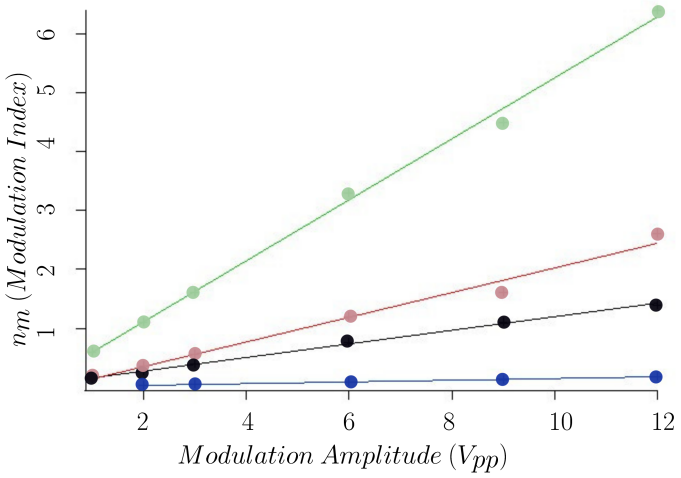

FIGURE 3.12: **Modulation index versus modulation amplitude.** The modulation frequencies used are $\frac{\omega_m}{2\pi}$=1MHz(green), 3MHz(red), 5MHz(black), 10MHz(blue). Measurements made with the peak ratio method

Then to recover n for each (ω_m, V) (modulation frequency and modulation amplitude) we have only to see how the modulation index n depends on ω_m at a fixed V (fig 3.13).

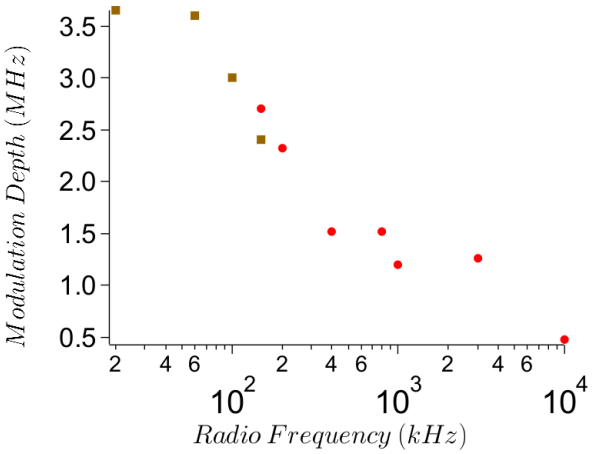

FIGURE 3.13: **Modulation depth ($\frac{\omega_d}{2\pi}$) versus modulation frequency.** Fixed modulation amplitude (2 V). Squares are measurements with the half width method, circles are measurements with the peak ratio method

When such a spectrum is sent to the AOM the resulting light spectrum will be the same of the RF except for a shift of the carrier frequency into the light domain, given by $\omega = \omega_0 - 2\omega_c$ (with the minus sign that accounts for the fact that we are using the -1 order). The double pass in the AOM produces a spectrum with the same ω_m but with doubled ω_d.
In fact if we suppose that a single pass has the effect

$$|\omega_0\rangle \rightarrow \Sigma_k i^k J_k(n_m)|\omega_0 + \omega_c + k\omega_m\rangle$$

where $|\omega\rangle$ is a photon state denoted by its frequency, then the second pass produces the state

$$\Sigma_k i^k J_k(n_m)|\omega_0 + \omega_c + k\omega_m\rangle \rightarrow \Sigma_{k,p} i^{k+p} J_k(n_m)J_p(n_m)|\omega_0 + 2\omega_c + (k+p)\omega_n\rangle$$

Renaming $k = K - p$

$$\begin{aligned} &= \Sigma_{K,p} i^K J_{K-p}(n_m)J_p(n_m)|\omega_0 + 2\omega_c + K\omega_m\rangle \\ &= \Sigma_K i^K J_K(2 \cdot n_m)|\omega_0 + 2\omega_c + K\omega_m\rangle \end{aligned}$$

where in the last step we Exploit the properties of the bessel functions, finding the expected result.

In our setup there is still a source of distortion due to the dependence of the AOM efficiency on the frequency; we neglect this effect when the modulation depth is less than the frequency range over which the AOM efficiency changes by a factor 20%. This range depends on the carrier frequency, usually it is on the order of 10-20MHz. In the cases where we are interested only in the dependence on the modulation depth at fixed total optical power we ensure that this is constant and don't consider distortion.
In the experiment the modulation parameters must be compared with the characteristic frequencies of the system: We expect that modulation can change the excitation dynamics only in the regime of a modulation depth greater than the laser linewidth $\omega_d > \gamma$.

Eventually, we verify that the atoms 'see' the spectrum we expect: in fig. 3.14 we report a frequency scan with modulated spectrum; the same experiment without modulation is reported for comparison. Even though we acknowledge the presence of distortion, we have verified that the spectrum that reaches the system is composed by a number of non-zero sidebands spaced by ω_m close to the one expected.

We verify that the system follows the variation of modulation also varying the modulation amplitude keeping the frequency fixed at resonance with a determined sideband (Figure 3.15). We have noted that the effective modulation depth is smaller than the expected one by a constant factor (about 1.3); we don't have any explanations for this behaviour yet and we limit to take this factor into account when we use frequency modulation on the system.

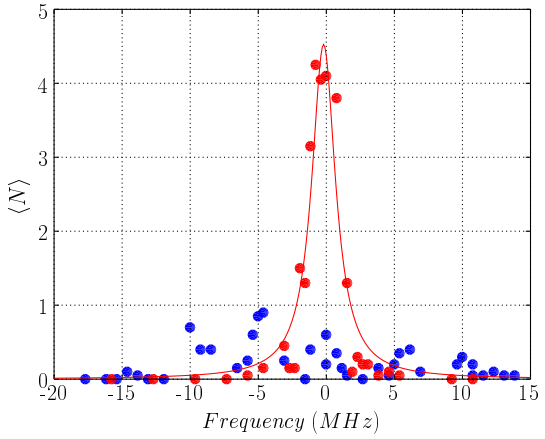

FIGURE 3.14: **Spectrum broadening with frequency modulation as seen by the atoms** Frequency scans: red points without modulation; blue points with a modulation of $\omega_m = 5MHz$, n_m=1.59. We verify the presence of different sidebands spaced by ω_m in the spectrum that is sent to the system.

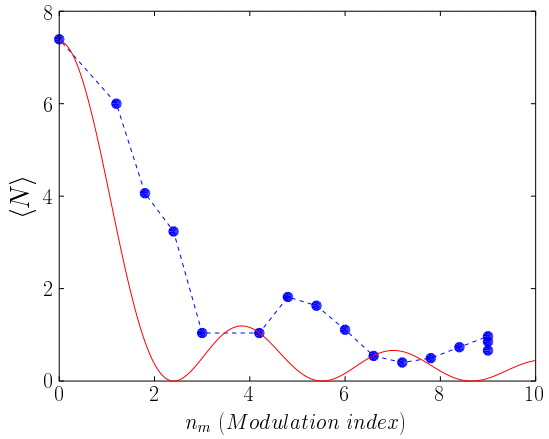

FIGURE 3.15: **Number of Rydberg excitations versus modulation index** Excitation frequency chosen on resonance with the carrier frequency. We expect the mean number of atoms to be proportional to $J_0(n_m)^2$. What we see is that the actual modulation index seen by the system is reduced by a factor ~ 1.3 whose origin is still uncertain.

3.5 Noise modulation

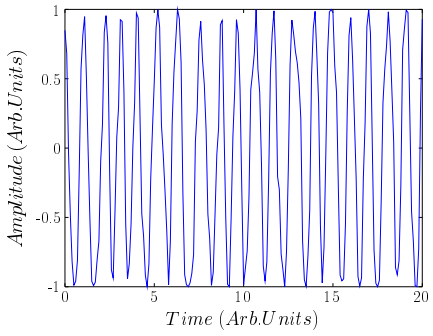

FIGURE 3.16: **Noise Modulation** The instantaneous frequency has fast fluctuations around a certain value.

When we use as the source of the modulation for the VCO a white noise the resulting RF will acquire a finite spectral width γ_{RF}. Combined with the laser linewidth this gives rise to a controllable artificial line broadening ($\gamma_{eff}^2 = \gamma^2 + \gamma_{RF}^2$); this is interesting because γ is a fundamental parameter in the dynamical quantities of our system, for example it enters the definition of the rate $\Gamma \sim \frac{\Omega^2}{\gamma}$ but also determines the width of the resonant shell for dynamics out of resonance (as seen in chapter 1).

The maximum broadening that we can obtain with this system (figure 3.17, about a factor 1.5 respect to the original spectral width) is not so large that it necessitates a

control of the angle (in the absence of the cat's eye it would give a displacement of the beam much less than the waist of the laser).

Noise modulation does not alter the total optical power too; it simultaneously lowers and broadens the lorentzian profile of the radiation spectrum.

This technique somehow extends the features of the modulation technique into a continuos regime and it is more similar to what happens with low modulation frequencies in the $\omega_m < \gamma$ regime where because of the finite linewidth the system can not distinguish the different sidebands.

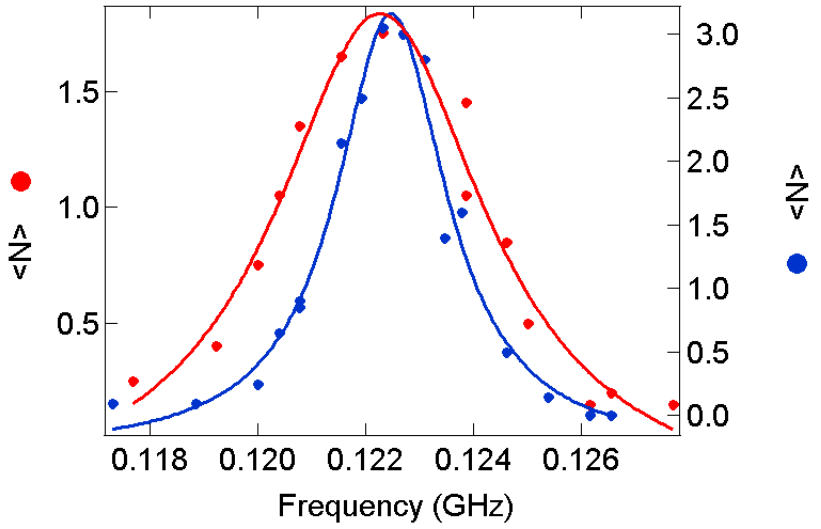

FIGURE 3.17: **Frequency scan with a noise modulation (red) and without (blue)**. We fit the two curves with lorentzian fits. The width increases as the height decreases

In this chapter we have presented the technical implementations of some multi-frequency techniques that the angle stabilization, provided by the cat's eye, makes possible. At this point, we imagine the confusion of the reader who has followed the explanations of the complexity of interacting Rydberg systems and has found that, in order to gain more information on such a system, we have decided to introduce new degrees of freedom in the excitation scheme. In the following chapters, where the experimental results of such methods are reported, we show how these techniques can simplify the picture of the particular aspect that is being studied.

Chapter 4

Results on the dynamics on resonance

As we have mentioned, the motivation for exploring multy-frequency techniques derives from the result obtained with the seed procedure, so it was natural trying to apply these techniques to the seed itself.
First, we devised a technical improvement of the preparation of the seed state which is about the suppression of the unwanted errors due to fluctuations of the reference which is used to keep fixed the lasers' frequencies. We briefly explain how these fluctuations arise in our technical setup and we show how noise modulation and sweeps techniques can reduce the effect of these fluctuations on the creation of seeds on resonance.

Then we want to extend the characterization of the seed technique to the regime of high seed number (up to a blockaded regime) studying how the number of seeds impacts on the facilitated process. In particular, we analyze the mean number of facilitated excitations in relation with the number of seeds. We show how this can be used to draw conclusions about the spatial configuration of the excitations (both seeds and facilitated ones); these results will be useful in the last chapter.

4.1 Seed stabilization

The seed technique allows the control of the trigger of the dynamics out of resonance which is a process characterized by high fluctuations. These fluctuations are an intrinsic feature of the highly-correlated system we are studying, but also the experimental

procedure can have fluctuations and both types of fluctuations will combine to give an effective fluctuation observed in the experiment.

A noisy experimental setup can then worsen the visibility of an effect on the statistics of a process.

The seed technique can suffer fluctuations which are inherent the experimental procedure, due to the method that is used to keep the lasers' frequency fixed, which functions as follows.

A reference laser is locked electro-optically to an atomic transition and it is sent to a Fabry-Perot cavity togheter with the $1012nm$ and $420nm$ lasers. A software receives the cavity output and sends correction signals to the $1012nm$ and $420nm$ laser in order to keep their frequency fixed respect to the reference.

Then we can have 'fast fluctuations' ($\sim kHz$) which are due to a bad lock of the reference (which can be caused by electrical noise or interference with other modes of the laser), and 'slow fluctuations' that are due to temperature changes in the laboratory ($\sim 10^{-3}Hz$) that influence the air refraction index that alters the apparent length of the Fabry-Perot cavity.

Fast fluctuations may occur during the time of a single shot ($\sim 25s$ for a shot of 100 repetitions), and therefore alter the statistics, slow fluctuations alter the experimental conditions from experiment to experiment.

The methods we are presenting reduce the effect of the fast fluctuations. We indicate with $\Delta\omega$ the standard deviation of the random variable $\omega(t)$. Fluctuations on the reference have a greater effect on the dynamics on resonance, and therefore on the seed, because they become relevant when the standard deviation becomes comparable to the laser linewidth $\Delta\omega \sim \gamma$ while the effect on a off-resonant dynamics becomes non-negligible only when the standard deviation $\Delta\omega$ is almost on the order of the detuning δ.

Note: in the ideal case of $\Delta\omega = 0$ and in the regime of small number of excitations the seed is still not deterministic because it is a poissonian process and thus have its own intrinsic fluctuations; we expect a Q value of zero in this case, which implies $< (\Delta N)^2 >=< N >$. We use the Q factor to quantify the stability of the seed we want to improve: the lower Q, the better the stability.
We are going to see how, using a broader excitation spectrum, we can achieve this.

4.1.1 Noise modulation

The noise modulation increases the spectral width to $\gamma_{eff} > \gamma$. Since the relative effect of fluctuations is given by the ratio $\frac{\Delta\omega}{\gamma}$, which is to say that they must be compared with the characteristic frequency of the excitation, a higher spectral width γ can be used to perform an excitation which is less sensitive to fluctuations.

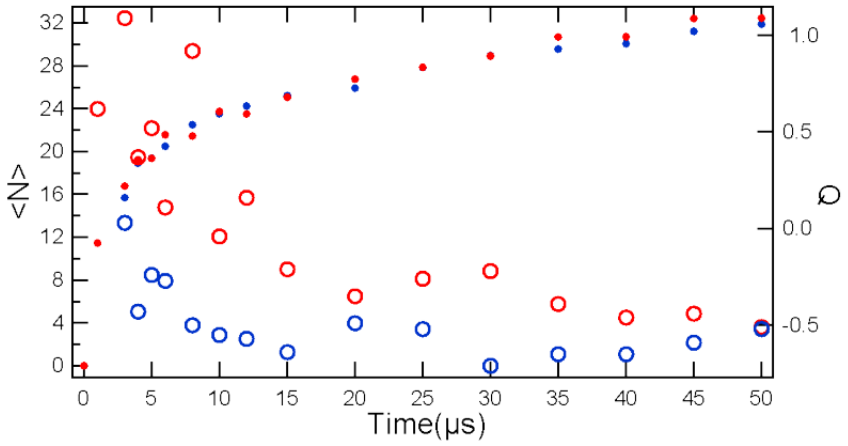

FIGURE 4.1: **Decrease of fluctuations with noise modulation** $\langle N \rangle$ (small points) and Q factor (empty circles) as a function of the time of the excitation on resonance without modulation (Red points) and with a noise modulation (Blue Points) in an artificial condition of high fluctuations. The Q factor becomes smaller with a larger spectral width. Counterintuitively, noise can be used to reduce fluctuations

Fig. 4.1 shows the number of excitations as a function of the excitation time with a frequency 'slightly' out of resonance; by this we mean that the frequency was chosen on purpose on the side of the lorentzian profile of the resonance where the effect of fluctuations on atoms is greater because of the non-zero derivative of the profile. The curve with a noise modulation, in the same conditions, has a lower Q factor, because of the decreased relative importance of the fluctuations in the determination of the resonance condition.

4.1.2 Sweep

Seed excitations can be created using a sweep across the resonance frequency. We explain why it should reduce fluctuations.

The instantaneous frequency $\omega(t)$ varies from repetition to repetition of a single shot in a range defined by $\Delta\omega$, due to fast fluctuations. It can be considered constant, though, during the time of the seed preparation, $\sim 1\mu s$.

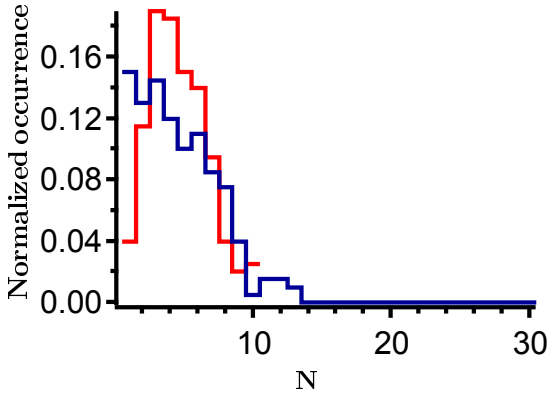

FIGURE 4.2: **Reduction of fluctuations for a sweep-generated seed** Counting histograms for a seed generated in an artificial condition of high fluctuations (Blue Bars, $\langle N \rangle = 3.56$, Q=1.22) and, in the same condition, with a sweep across the resonance frequency (Red Bars, $\langle N \rangle = 3.58$, Q=0.2). The sweep-generated seed has lower fluctuations around the mean value.

With a sweep over a range greater than $\Delta\omega$, we can be sure that there is a moment during the sweep where the resonant condition is matched.

Since the sweep we have characterized (as seen in chapter 2) are linear, this means that the time spent on resonance does not depend by the actual realization of $\omega(t)$ during that particular repetition. To obtain time of resonance, we can use the estimation $\gamma(\frac{\Delta\omega_{sweep}}{\Delta t})^{-1}$ which is the time that the sweep with slope $\frac{\Delta\omega_{sweep}}{\Delta t}$ needs to cross a laser linewidth.

We choose the sweep direction in order to make the laser frequency vary from a blue detuning to a red detuning, in order to avoid interaction-facilitated excitations that could follow the resonant excitation. In fig. 4.2 we compare the counting histograms of a 'slightly out of resonance' seed and of a sweep-generated seed of equal mean number. In the first case we have higher occurrence of values higher and lower than the mean number, while the excitation performed with the sweep becomes again poissonian (as it is demonstrated by the lower Q factor).

4.2 High seed number

Previous works on the seed have made use of a mean number of excitation on resonance around $1-2$ seeds, just enough to be sure that the probability of having no excitations was much smaller than the probability of having at least one. This has been done in the optics of studying the triggering of the off-resonant dynamics. Now we want to investigate what happens when we start from a high seed number, which is to say from a situation that is already blockaded. The motivation are related to the intuition that

this could give information about the spatial configuration of the excitations, both on resonance and out of resonance.

We explain better: we expect two contrasting effect to be at play with an high seed number. On the one hand, each atom created on resonance contributes to the growth of the facilitation volume, therefore should increase the number of facilitated excitations. On the other hand, we can not say exactly how close the excitations are in a blockaded situation, but only make an estimation based on the interaction volume and the volume of a blockade sphere; if the excitations were so close that also the dynamics out of resonance result we would expect the opposite effect, which is to say that also the dynamics out of resonance is blockaded.

Moreover, the two type of excitations have two different dependence from the density and this fact too could give information about the spatial configuration of the excitations. Infact, due to the dipole blockade, the dynamics on resonance has a weak dependence on the density and we expect that the excitation it creates are more uniformly distribuited. Instead the dynamics out of resonance depends strongly on the density because of the dependence on the number of atoms in the facilitation shell; in this case we expect that excitations created off-resonantly are localized in the higher density zone.

The angle stability guaranteed by the cat's eye allows the best condition to observe an eventual effect because the interaction volume is the same for both resonant and off-resonant dynamics.

The experiment is conducted as follows. We change the number of seeds varying the duration of the resonant pulse.

After the seed phase the IR frequency is switched out of resonance, with detuning in the range $20 - 30MHz$), for a fixed time. We used 1D configuration because here we have a simpler picture of the blockade which acts along only two directions. We analyze the numbers $\langle N_{fac} \rangle$ and $\frac{\langle N_{fac} \rangle}{\langle N_{seed} \rangle}$ versus $\langle N_{seed} \rangle$.

The ratio $\frac{\langle N_{fac} \rangle}{\langle N_{seed} \rangle}$, shows that indeed we don't have an independent avalanche for each seed, but that given enough time for the out of resonance radiation to reach saturation all the chains start interacting (and blockading) with each other.

We have found that the relation between $\langle N_{fac} \rangle$ and $\langle N \rangle$ is not monotonic but there is a certain seed number above which $\langle N_{fac} \rangle$ decreases; we interpret this with the fact that as the interaction volume is filled with seeds less space is left for facilited excitations in it.

In particular we have found that this inversion happens for a number of seeds $\langle N_{seed} \rangle$ that corresponds to a mean distance between seeds which is about $2r_{fac}$. This is indeed

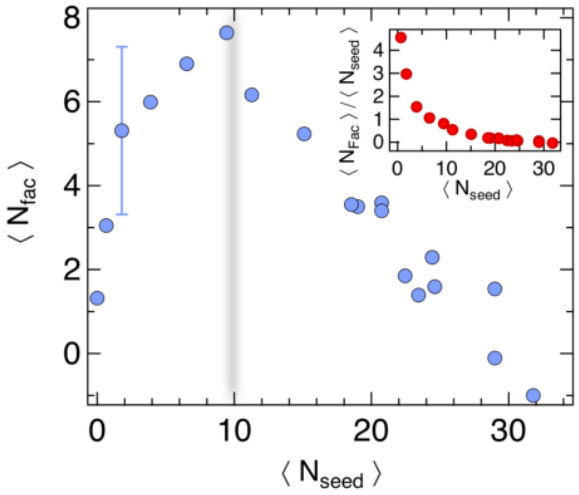

FIGURE 4.3: **Number of facilited excitations as a function of the number of seeds.** A high number of seeds can block the dynamics out of resonance: the number of facilitated excitations has infact a maximum and then, increasing the number of seeds, decreases. N_{fac} and N_{fac}/N_{seed} vs N_{seed}

the condition by which, in a ideal 1D situation, adding a seed between two excitation at that distance cause a blockade of an off-resonant excitation.

In conclusion, we have demonstrated that excitations on resonance can produce an effect on blockade also on the dynamics out of resonance. Moreover, we have got indications that the deviation from a perfect 1D system is small. This is going to be of help in the last chapter where we will use simulations with perfect 1D systems.

Chapter 5

Results on the dynamics out of resonance

Density of the MOT (ρ) and detuning (δ) play a fundamental role in the dynamics out of resonance, because they determine the number of atoms in the facilitation volume ($\tilde{N}$).

We briefly review the simple, one dimensional, model which highlights this role and has been used for qualitative comparison with experimental results. We refer to this model as 'static', because it neglets the dynamics of the external degrees of freedom of the atoms (frozen gas approximation).

Using the techniques described in chapter 3, we can obtain an artificially greater linewidth γ, which, according to the static model, should results in a greater facilitation volume V_{fac} or, equivalently, simulate a greater density. During this work of thesis this hypothesis was subjected to experimental verification.

Since the results seem to indicate instead that there is no clear dependence of the dynamics on γ, we develop another model which takes into account also the external degrees of freedom ('dynamic model') and explains the experimental results.

Description of this model, implications and future experiments are discussed.

5.1 Static model for the out of resonance dynamics

The static model allows a prediction for the counting histograms $P(N)$ (and consequently $\langle N \rangle$ and Q) for a 1D chain of facilitated excitations given the MOT profile, the detuning

of the driving laser and the laser linewidth γ. The resulting counting histograms can be used for qualitative comparison with experimental histograms.

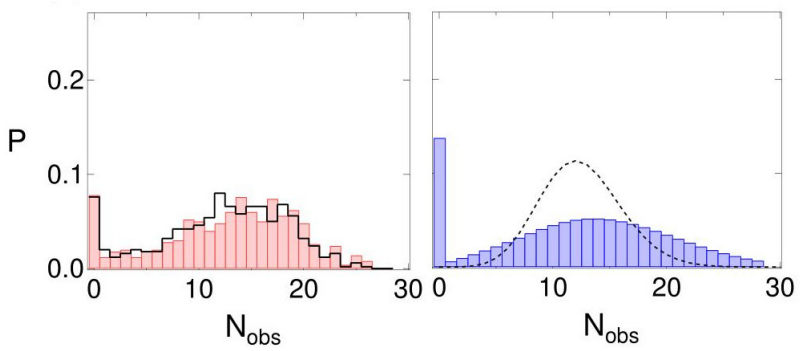

FIGURE 5.1: **Experimental and simulated counting histograms** Experiment (left): the same $\tilde{N}$ generated with two different combinations of ρ and δ gives a similar result (red bars and black lines). Simulation (right): with the same experimental parameters and accounting for the finite detection efficiency (bars); dashed line is the real counting distribution.

The chain can start with a seed, that we can have with a certain probability P_{seed}, in the center of the MOT.

We consider the probability of finding at least one atom in the facilitation volume; in this case we excite it with probability 1. De-excitation processes or non-facilitated dynamics are completely neglected.

The probability of excitation is then $1-e^{-\tilde{N}(r_{fac})}$; infact $e^{-\tilde{N}}$ is the probability of finding no atoms given a poissonian distribution of the number of ground state atoms in the facilitation volume with mean equal to $\tilde{N}(r) = \rho(r)V_{fac}$.

ρ_r may be taken to be gaussian $\rho(r) = \rho_0 e^{-\frac{r^2}{2\sigma^2}}$ with width σ and peak density ρ_0.

After the excitation the facilitation volume shifts and is located at a distance r_{fac} from this second excitation, and the process can be iterated. We consider dynamics occuring only in one direction for simplicity.

The probability of realizing N excitations $P(N)$ then becomes simply the product of P_{seed} and the probability of taking the other $N-1$ steps (for a total of N with the seed one), multiplied by the probability of not taking the $N+1$ step:

$$P(N) = P_{seed} \cdot \Pi_{n=1}^{N-1}(1 - e^{-\tilde{N}(nr_{fac})}) \cdot e^{\tilde{N}(Nr_{fac})} \tag{5.1}$$

We consider only N which satisfy $N - 1 < t_{exc}\Gamma$ which is to say the maximum number of steps occuring at a rate Γ in a total excitation time t_{exc}.
The major implication of this model is the different role played by ρ and γ, on which

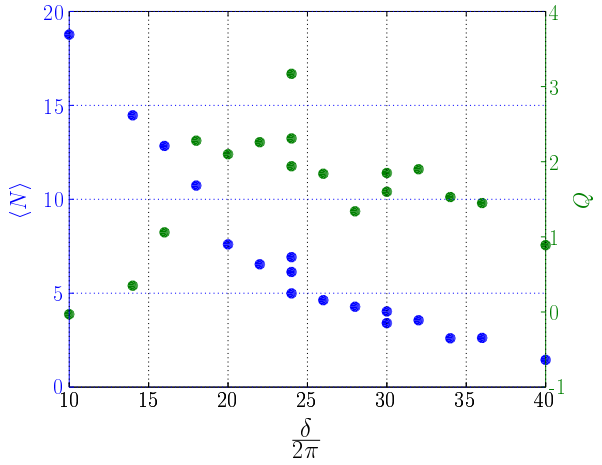

FIGURE 5.3: **Experimental dependence of the mean number and Q factor on the detuning** There is a qualitative agreement with the prediction (figure 5.2) of the static model that reproduces both the decrease of the mean number and the peak of the Q factor. 1D geometry, $\langle N_{seed}\rangle = 0.8$, $\frac{\Omega}{2\pi} = 1MHz$, $\sigma_x = 120\mu m$, $\sigma_y = 90\mu m$, $\rho_0 = 10^{11}\frac{A}{cm^3}$, $\tau = 100\mu s$.

P_N depends almost exponential-like, and by Γ which plays only a marginal role beacuse it determines only the maximum number of steps that can be taken. For long times (or high Γ) ($t_{exc} \gg \frac{\sigma}{\Gamma r_{fac}}(ln(\rho(0)V_{fac}))^{\frac{1}{2}}$) this in fact means the we are starting to consider chains whose last steps are very unlikely, and therefore do not alter significantly the probability distribution.

These dependences from the dynamical parameters could be generalized also the 3D case, although here we don't dispose of an equally simple model.

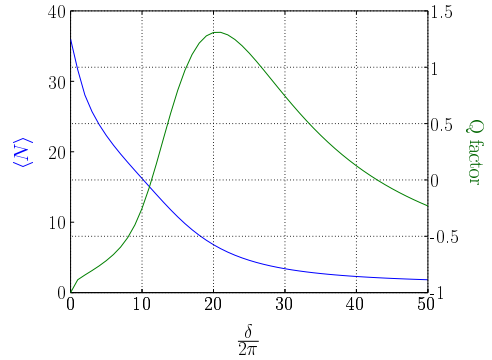

FIGURE 5.2: **Simulation of the dependence of the mean number and the Q factor dependence from the detuning** The static model predicts a decrease of the mean number and a peak of the Q factor as the detuning increases. $\rho = 10^{11}\frac{A}{cm^3}, \sigma = 50\mu m$, $\langle N\rangle = 1$

From $P(N)$, we can find $\langle N\rangle$ and Q. If we plot them in function of the detuning (figure 5.2) we see that $\langle N\rangle$, as expected, decreases with δ while Q has a peak in the transition

zone between efficient-inefficient avalanche process. An efficient avalanche process produces chains longer than the MOT width the majority of the times, while an inefficient one doesn't. We expect that both situations have a low Q while the transition regime must have an higher one because of the occurence of high and low N realizations with a similar weight.

We can see that this trend is confirmed by the experiment (5.3).

In figure 5.4 we plot the mean number in function of the detuning for different values of the facilitation volume, in order to give an idea of the expected effect of an artificial broadening according to the model we have just presented. We introduce the parameter β which is the ratio between the increased facilitation volume and the original one V_{fac}^{eff}/V_{fac}.

Since the transition between efficient-inefficient avalanche is characterized by a variation of both $\langle N \rangle$ and Q we expect this to be the ideal experimental regime to test our idea studying the dependence on β.

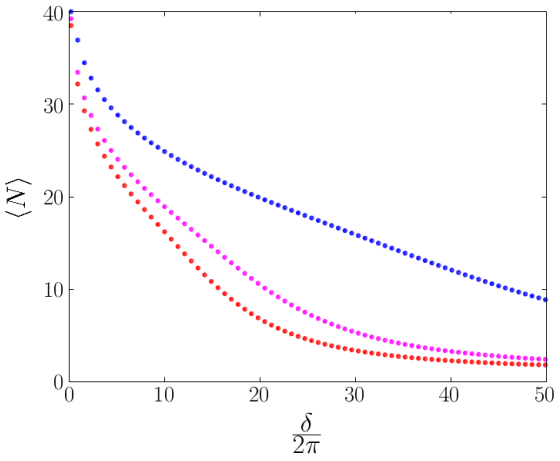

FIGURE 5.4: **Simulation for different values of the facilitation volume.** Expected effect for different $\beta = \frac{V_{fac}}{V_0}$. $\beta = 1$, same parameters of figure 5.2,(red), $\beta = 1.5$ (pink), $\beta = 5$ (blue).

5.2 Experiment

The techniques of noise and frequency modulation can help to produce a greater V_{fac}. With noise modulation and in the regime of low modulation frequency infact we have a greater linewidth γ because the spectral width is increased.

In the case of high modulation frequency we have a spectrum composed by different frequencies; then the facilitation volume becomes the union of the facilitation volumes that each of those frequencies would have by its own.

We estimate β (ratio between the increased facilitation volume and the original one) using $\beta = \frac{\gamma_{eff}}{\gamma}$ for the noise modulation case and $\beta = \frac{\omega_d}{\gamma}$ for the low modulation frequency case ($\omega_m < \gamma$). Basically we are using the ratio between the increased spectral width and the original one. Instead, in the high modulation frequency regime ($\omega_m > \gamma$) we use $\beta = 1 + 2n_m$ ($\sim$ number of sidebands significantly different from 0).

β ranges from ~ 1.5 (in the case of noise modulation, as seen in chapter 3) to $\sim 5 - 7$ (frequency modulation). Both techniques, as we have seen in chapter 3, don't influence the total optical power.

The experiments are performed under different conditions: the parameters of the system we vary are MOT density, detuning, laser power, number of seeds, excitation time.

Peak density has been varied from $\sim 10^{10}$ to $\sim 10^{11} atoms/cm^3$ and δ from $\sim 10MHz$ to $\sim 50MHz$; $\tilde{N}(0)$ was estimated to be $\sim 1 - 4$. The density was varied by changing the magnetic quadrupole intensity that determines the width of the MOT with the consequence that to have a denser MOT one has to use a smaller one. The minimum MOT width used has been about $40\mu m \sim 8r_{fac}$, enough to produce a chain of excitations of a measurable number of atoms.

Typical Ω_{Ryd} used varies from $2\pi \sim 100kHz$ to $2\pi \sim 700kHz$ (with a maximum Γ of $2\pi 0.7MHz$ then). We choose 'high' excitation times, that allow for a chain whose elements are formed with a rate Γ to cover the MOT width; a typical 'high' time is $\sim 100\mu s$.

We investigate both avalanche with seed and without (when the avalanche is triggered by 'spontaneous' seeds that are formed out of resonance). The issue with the spontaneous seeds is that, although their dynamics doesn't depend on β, as long as we keep $\gamma_{eff} < \delta$ (avoiding portions of the spectrum to come near resonance), in principle they could decrease the relative importance of the effect we are trying to observe.

For this reason, we always check that the value of the Q factor is high ($\gtrsim 2$); we cannot know whether the avalanche was started by an artificial seed or by a spontaneous one but we have the confirmation that a facilitated process is happening.

The experiment is carried out in this way: after we fix all the parameters we have just explained we choose the detuning that maximizes the Q parameter (the region of maximum expected effect, as we said before). We study how the mean number and the Q factor vary for different values of β, obtained with the techniques explained. What we find is that neither $\langle N \rangle$ or Q undergo a variation above the level of fluctuations.

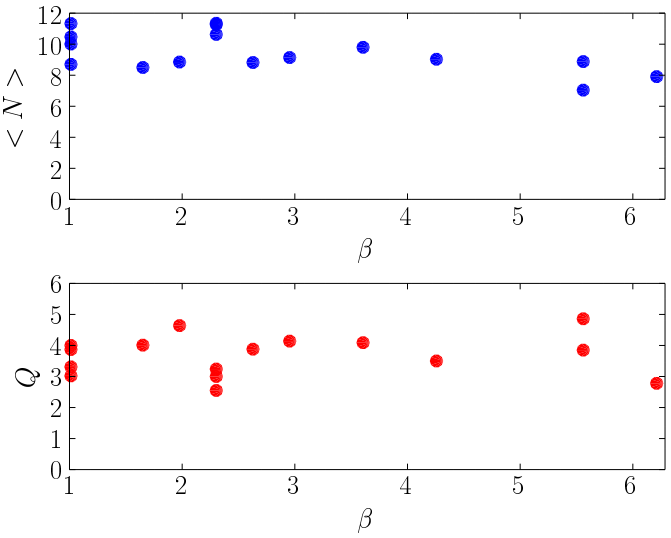

FIGURE 5.5: **Experimental Dependence on the artificial manipulation of the facilitation volume** 3D configuration, $\frac{\delta}{2\pi} = 46MHz$, $\frac{\omega}{2\pi} = 3.5MHz$, $\langle N_{seed} \rangle = 0$, $\tau = 100\mu s$, $\frac{\Omega}{2\pi} = 660kHz$, $\sigma_x = 150\mu m$, $\sigma_y = 120\mu m$

Then we try to reproduce the scaling of fig. 5.4 by studying how the dependence on the detuning is affected by a $\beta \neq 1$. This experiment does not show a relevant effect produced by a variation of β.

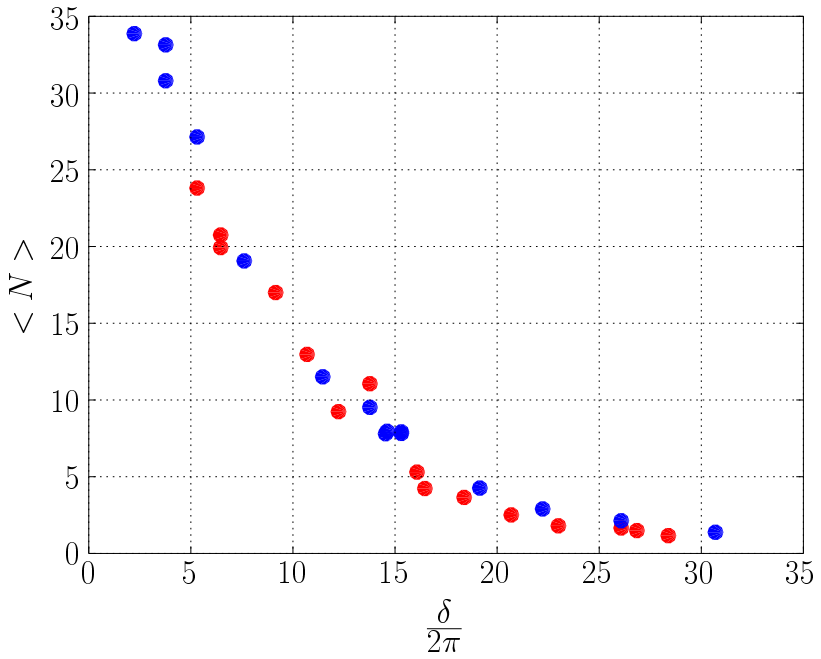

FIGURE 5.6: **Experimental Dependence of the mean number on the detuning with and without noise modulation** 1D configuration, $\langle N_{seed} \rangle = 0$, $\tau = 50\mu s$, $\frac{\Omega}{2\pi} = 2.2MHz$, $\tau = 50\mu s$, $\sigma_x = 132\mu m$, $\sigma_y = 99\mu m$. Red points have no modulation, blue points have a noise modulation. The increased facilitation volume does not reproduce the scaling predicted by graph 5.4

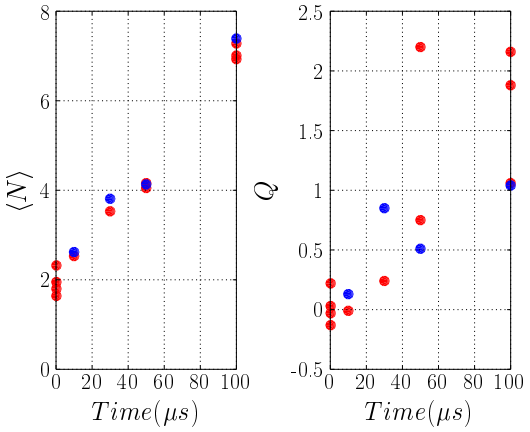

FIGURE 5.8: **Dependence of $\langle N \rangle$ and Q on the excitation time with and without a modulation with a high modulation frequency** 1D configuration, $\frac{\delta}{2\pi} = 20MHz$, $\langle N_{seed} \rangle = 2$, $\frac{\Omega}{2\pi} = 250kHz$, $\sigma_x = 40\mu m$, $\sigma_y = 30\mu m$, Red points without modulation, blue points with modulation $\frac{\omega_m}{2\pi} = 2.5MHz, n_m = 1$

We have found that β doesn't have a relevant impact on $\langle N \rangle$ and Q for high excitation times, the regime where the predictions of the static model were based.

Now we want to study how β affects the dynamics even for small times, to see if it has a role in the way the state we find for high times is reached. We perform experiments where we compare the curves in function of the excitation time with $\beta = 1$ and $\beta \neq 1$, finding that also in this case β does not alter the dynamics (figures 5.7,5.8,5.9).

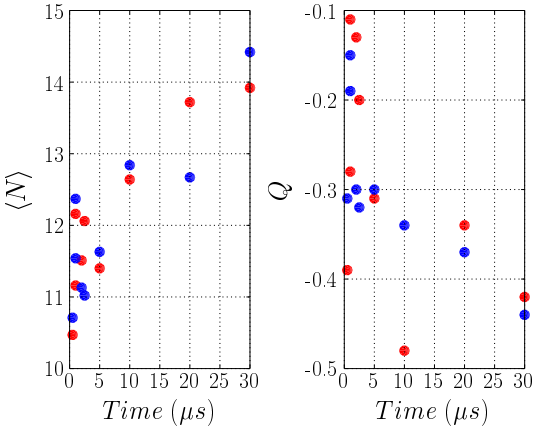

FIGURE 5.7: **Dependence of $\langle N \rangle$ and Q on the excitation time with and without a modulation with a low modulation frequency** 1D configuration. $\frac{\delta}{2\pi} = 12MHz$, $\langle N_{seed} \rangle = 11$, $\frac{\Omega}{2\pi} = 1MHz$, $\sigma_x = 12.6\mu m$, $\sigma_y = 12\mu m$. Red points without modulation, blue points with modulation $\frac{\omega}{2\pi} = 100kHz$, $n_m = 34$.

[H]

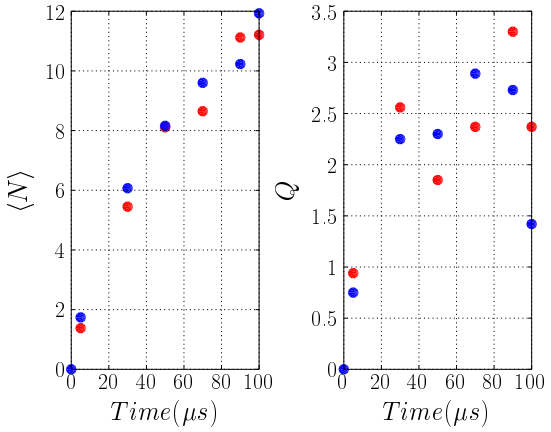

FIGURE 5.9: **Dependence of $\langle N \rangle$ and Q on the excitation time with and without a noise modulation** 1D configuration, $\frac{\delta}{2\pi} = 20MHz$,$\langle N_{seed} \rangle = 0$, $\frac{\Omega}{2\pi} = 2.2MHz$, $\sigma_x = 132\mu m$, $\sigma_y = 99\mu m$. Red points without modulation, blue points have noise modulation.

We have seen that increasing artificially the facilitation volume does not influence relevantly, as expected, the facilitated dynamics.

The study of the curves made varying the excitation time has also a stronger implication, which follows from the this consideration. We have used techniques that don't alter the total optical power, which is to say that when we increase the spectral width of the light we spread this power over a larger range. Since the system doesn't react to this spread, this suggests that the relevant dynamical parameter should be related to the optical power alone. In the next chapter we present a possible explanation for this behaviour, that takes into account this suggestion.

5.3 Dynamic model

The static model assumes that atoms don't move considerably during the time of the experiment: this is true when we compare the mean displacement due to thermal motion in a typical experiment time to the blockade radius ($\sim 10\mu m$), but out of resonance the smallest natural length is the facilitation shell width which is more than two orders of magnitude smaller.

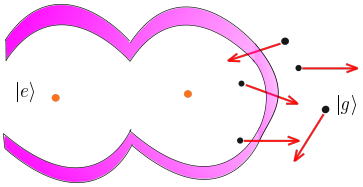

FIGURE 5.10: **Representation of the atomic motion in and out of the facilitation volume.** Ground state atoms at thermal speed cross the facilitation volme in a time shorter than the characteristic time of the internal variables

For our typical excitation rate Γ, moreover, the interaction time t_{int} (time spent in the facilitation volume) is much less than the excitation time ($\sim \Gamma^{-1}$); finding an atom in the facilitation volume then is not enough to excite it with considerable probability. For example $\delta = 20MHz$ implies $\delta r = 33nm$; an atom which travels at thermal motion (V_{TH}, about $0.2\mu m/\mu s$ for $T = 150\mu K$)) needs only $165ns$ to cross it, while our typical Γ doesn't reach $1MHz$.

Starting from these considerations, we derive the probability of a facilitated excitation considering the thermal motion and an incoherent process, finding that the dependence on the linewidth γ (and consequently the gain in the facilitation volume β) is canceled.

Since $\Gamma t_{int} \ll 1$ an atom that passes through the facilitation volume than has only a small probability of being excited P_{exc} which can be deduced from the master equation: $\partial_t P_{exc} = \Gamma(t)(P_N - P_{exc})$
where P_N is the probability of having a configuration of N excitations that generate a facilitation volume through which our atom is passing. Since $P_{exc} \ll 1$ we neglet it on the right side and, approximating $\Gamma(t) = \Gamma_0$ during t_{int} (and 0 elsewhere) and integrating we find $P_{exc} = \Gamma_0 t_{int}$.

There is though a continuos flux of atoms through the facilitation shell that then have a similar (small) probability of being excited.

Leaving out considerations about the angle and the thermal speed which add complications but don't change the order of magnitude of the parameters at play, we use an average interaction time $\tilde{t}_{int} \sim \frac{\delta r}{v_{TH}}$.

Then if we want to find how the probability of making a facilitated excitation varies with time we have to consider a flux of atoms through the shell which is $\Phi = \frac{\tilde{N}}{\tilde{t}_{int}}$

(with $\tilde{N} = \rho V_{fac}$). Notice that Φ does not depend on γ, because both $\tilde{N}$ and $\tilde{t}_{int}$ are proportional to it.

Then fixed a configuration of N excitations, we have $\partial_t P_{N+1} = P_M P_{exc} \Phi$ which is to say that the effective rate becomes:

$$\Gamma' = P_{exc}\Phi = \Gamma \rho V_{fac} \tag{5.2}$$

substituting the definitions.

What this formula says is: the effective rate is the product of the single-atom rate multiplied by the mean number of atoms that are resonant.

The dynamics is described only by Γ' which does not depend on γ: infact γ appears in $V_{fac} \sim \gamma$ and in $\Gamma \sim \gamma^{-1}$ therefore its contribution is canceled. This explains also why the curves in function of the excitation time seemed not to be affected by the variation of β. Also the dependence on $\tilde{t}_{int}$ is canceled, and consequently that on the thermal velocity.

Although the expression for the effective rate Γ' seems simple, Γ' depends on V_{fac} which in turn depends on the atomic configuration, so extending this reasoning to a generalized master equation is a work which has not been done yet and has its own amount of theoretical and numerical investigation and goes beyond the purpose of this thesis,

Since Γ' contains the same dependence on Ω^2 (total optical power) and ρ this predicts the same scaling for a variation of each of them; the experimental verification of this prediction is going to provide a first observation of the validity of this model.

5.4 Considerations on a coherent treatment

We have so far assumed facilitated dynamics to be an incoherent process; this doesn't quite agree with the comparison of the mean interaction time ($\sim 100ns$) and the coherence time (which can be estimated using $\gamma^{-1} \sim 1 - 2\mu s$).

We present a simple reasoning that shows that the assumption a completely coherent process doesn't alter the main results obtained so far.

In this case we can suppose that an atom who is passing through the facilitation volume and starts a Rabi oscillation, using the approximation of small interaction times, gets a $P_{exc} = \alpha\Omega^2$. α is a constant which we can not determine now but we expect it is related to the velocity of the atom that is the only dynamical parameter that remains since in the coherent regime the linewidth γ doesn't play any role. When we substitute this P_{exc}

into eq. (5.2) we find once again an effective rate which doesn't depend on γ, and that is proportional to ρ,V_{fac}/γ and Ω^2.

The dependence on Ω^2 is worth to be further examined: in a dynamics described only by Γ' the physical quantities evolve as functions of $\Omega^2 t$. This may sound strange because a coherent dynamics is usually described by functions of Ωt; the origin of this behaviour as we have seen is in the thermal motion.

To distinguish a coherent from an incoherent dynamics, on resonance, this experiment is usually performed: different time dependences for different Ω are taken, then the time axis is rescaled using Ω or Ω^2. The zone of the curves where the dynamics is coherent would collapse togheter with the Ω scaling, the zone of the curves where the dynamics is coherent would collapse togheter with the Ω^2 scaling.
The above results mean that such a method cannot be used to distinguish between the two in the dynamics out of resonance, because also a coherent process would scale with Ω^2.

5.5 Conclusions

In this chapter we have shown the results of the artificial manipulation of the facilitation volume, which is a relevant quantity that governs the off-resonant excitation dynamics. This manipulation was achieved through a larger effective spectral width (γ) of the laser field. We have found that, because of the disorder induced by the thermal motion ($v_{TH} \sim 0.2\mu m/\mu s$) the spectral width loses its importance and its variation doesn't influence the dynamics. The thermal motion becomes relevant when dealing with the dynamics out of resonance because the smallest natural length scale is the width of the facilitation volume, which is crossed by atoms at thermal velocity in a time much shorter than the inverse of the excitation rate.

This conclusions were drawn after the work of analysis of the experimental data.

Since we derived a model which predicts the same scaling for quantities like Ω^2 and ρ the validity of this model can be tested in the next future.

We also suggested that the thermal motion must be taken into account when estimating the degree of coherence of the facilitation process; infact it determines the interaction time which must be compared to the coherence time to determine if a coherent or an incoherent dynamics prevails.

Chapter 6

De-excitation dynamics

Before reporting the experimental results of the de-excitation, an additional premise on the theoretical framework we use to describe the de-excitation dynamics is necessary, so we briefly sketch the theory of a two-level system with a loss from one of the states.

We study experimentally how the interactions modify this picture and we show how this mechanism can be used to gain information on a system which has been subjected to Rydberg excitation.

In particular, de-excitation permits a sort of spectroscopy which allows to investigate the interactions between Rydberg excitations. We find results in good agreement with the ones obtained in previous works on the excitation dynamics but we present also completely new results.

Then we study de-excitation dynamics, finding that it is somehow specular to the excitation dynamics and again we find agreement with previous results and report the new aspects that have emerged. Moreover, we find evidence that de-excitation dynamics can be used to increase the accuracy of the preparation of states with particular spatial distributions demonstrating that de-excitation is not only an investigative tool but also an active method that can be used to control complex many-body systems.

The experiment performed with the 1D geometry show a good agreement, to a qualitative level, with numerical simulations performed by Guido Masella and we use them to confirm the validity of our interpretation.

6.1 Theory

De-excitation dynamics is a highly correlated process, as excitation dynamics, because of the interactions between Rydberg atoms so it useful to show the theory for a non-interacting two-level system with a channel of loss that provides a basis for the understanding of de-excitation when, during the presentation of the experimental results, the interactions will be added.
We have $|70s\rangle = |1\rangle$ and $|6p\rangle = |0\rangle$ which decays spontaneously with a mean lifetime $\tau_{6p} \sim 120ns$ to the $|5s\rangle$ which is no more coupled with any other level.

In the rotating frame we have the hamiltonian

$$H = \frac{\delta}{2}\sigma_z + \frac{\Omega}{2}\sigma_x$$

where δ is the laser detuning respect to the $6p \to 70s$ transition and $\Omega = \Omega_{1012nm}$.

H, together with an incoherent term L_{6p} due to the decay of the $|0\rangle$ state dictates the evolution of the matrix density ρ:

$$\partial_t \rho = i[\rho, H] + L_{6p} \tag{6.1}$$

where

$$L_{6p} = \frac{1}{\tau_{6p}} \begin{pmatrix} -\rho_{00} & -\frac{1}{2}\rho_{01} \\ -\frac{1}{2}\rho_{10} & 0 \end{pmatrix}$$

The incoherent term produces a loss of atoms which exit from the system and a decay of coherences between the Rydberg and the intermediate level. We leave out the finite laser linewidth as source of decoherence since the coherence time of the laser ($2-3\mu s$) is much greater than $\tau_{6p} \sim 120ns$. For the same reason, we also neglet spontaneous decay from the Rydberg state ($\tau_{70s} \sim 150\mu s$).

In general the exact solution for ρ_{11} will contain also a trace of Rabi oscillations, beside the decay induced by the intermediate level. We are interested in the solution in the incoherent limit then, which is to say $\frac{1}{\tau_{6p}} \gg \Omega$, because in this regime the Rabi oscillations are istantly damped and we find a simpler solution, which is more useful in comparison with the experimental results, especially when in a regime of interacting particles.

We are going to use a notation similar to that of the excitation in order to stress the symmetry between excitation and de-excitation; in this case we define $\gamma = \frac{1}{\tau_{6p}}$.

Under the incoherent condition we neglet the coherences and we describe the evolution of the populations, following a treatment anologue to [9] with a master equation for the

reduced density matrix μ, which has only diagonal entries:

$$\partial_t \mu = \Gamma(\sigma_x \mu \sigma_x - \mu) - \gamma|0\rangle\langle 0|\mu \tag{6.2}$$

with $\Gamma = \Gamma_0 \frac{1}{1+(\frac{\delta}{\gamma})^2}$ and $\Gamma_0 = \frac{\Omega^2}{\gamma}$.

We can rewrite equation. 6.2 in the form: $\partial_t \begin{pmatrix} \mu_0 \\ \mu_1 \end{pmatrix} = \begin{pmatrix} -\Gamma - \gamma & \Gamma \\ \Gamma & -\Gamma \end{pmatrix} \begin{pmatrix} \mu_0 \\ \mu_1 \end{pmatrix}$ which has solutions of the form $\mu_1(t) = \alpha_1 e^{\lambda_+ t} + \beta_1 e^{\lambda_- t}$ (and a similar one for μ_0, with the initial condition that is satisfied imposing $\alpha_i + \beta_i = \delta_{i1}$) where $\lambda_\pm = -\Gamma + \frac{1}{2}(-\gamma \pm \sqrt{(\gamma^2 - 4\Gamma^2)})$ are the eigenvalues of the last matrix. In the approximation $\gamma \gg \Gamma$ (automatically satisfied if $\gamma \gg \Omega$) we can see that $\lambda_+ \sim -\gamma$ and $\lambda_- \sim -\Gamma$.
Then finally one finds

$$\partial_t \mu_1 = \rho_{11} \sim e^{-\Gamma t} \tag{6.3}$$

where we have neglected the contribution of the other exponential because it decays with a rate faster than the minimum time interval we are interested in resolving in the experiment and because $\frac{\alpha_1}{\beta_1} \sim \frac{\Gamma}{\gamma}$, and we put $\beta_1 = 1$ in order to match the initial condition. ρ_{11} is the only observable accessible with our experimental setup, and so equation 6.3 constitutes our reference.

What happens when interactions come into play?
What we expect is that we can use a master equation similar to the one ([9]) which describes the excitation process:

$$\partial_t \mu = \Sigma_k \Gamma_k (\sigma_x^k \mu \sigma_x^k - \mu) - \gamma \Sigma_k |0\rangle^k \langle 0|^k \mu \tag{6.4}$$

where since the index k runs on the atoms which are in the Rydberg state when de-excitation begins and

$$\Gamma_k = \Gamma_0 \frac{1}{1 + (\frac{1}{\gamma}(\delta - V_k)^2} \tag{6.5}$$

Γ_k is the rate of de-excitation of the k atom, whith V_{int} its vdW potential. The evolution of the internal states of the atoms is still correlated and impossible to solve analitically, but a first difference between excitation and de-excitation is the number of atoms involved, which can be $\sim 1000 - 10000$ in the first case and ~ 10 in the second one (in typical cases of our experiments). This allows a speed-up of the numerical simulations which we use in the course of this chapter for comparison with the experimental results and for confirmation of the hipothesis we present. Another important is the one-way direction of possible transitions: in the excitation dynamics, the laser coupling can induce both transitions $|0\rangle \to |1\rangle$ and $|1\rangle \to |0\rangle$ while the de-excitation dynamics induces

only $|1\rangle \rightarrow |0\rangle$ transitions in the approximation, valid in the incoherent regime, that an atom which ends in the $|0\rangle$ state is istantly removed from the system.

6.2 Experimental Procedure

In order to perform de-excitation, some of the parameters of excitation have to be chosen in a more narrow range than in other experiments. Here we explain why this is necessary.

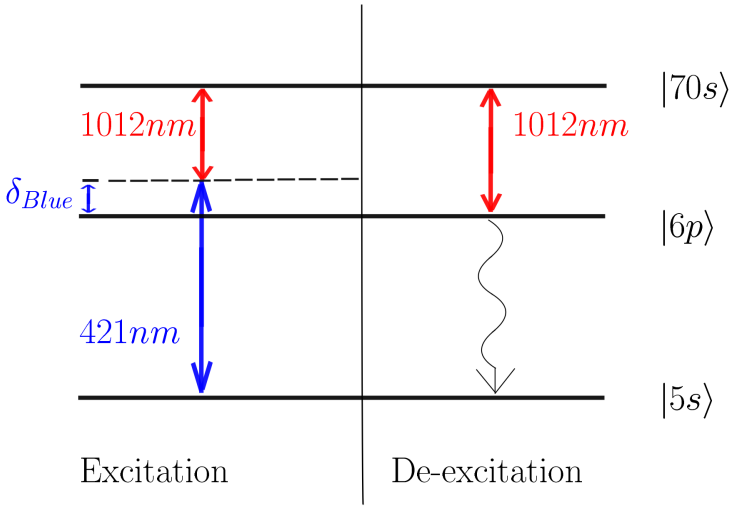

FIGURE 6.1: **Excitation and de-excitation scheme.** When the $1012nm$ laser switches frequency it couples the Rydberg state with the level $6p$ which decays fast to the ground state ($\sim 120ns$), starting the de-excitation phase.

A de-excitation experiment is composed by two parts; the first one prepares the state composed by some Rydberg excitations that are subject to de-excitation in the second part.

As we have already explained in the technical chapter this requires a frequency switch of the $1012nm$ laser that is performed with a change ("jump") of a RF sent to an AOM. This implies that we have to choose a detuning of the $421nm$ laser (needed for the excitation part) from the $6p$ state not higher than $60MHz$, the frequency range where the AOM can diffract efficiently (as we explained chapter 2): infact from the satisfaction of the resonance condition for the excitation and the de-excitation we see that the jump (from a resonant excitation to a resonant de-excitation) should be equal to δ_{Blue}. The frequency jump and δ_{Blue} must have the same sign.

This δ_{Blue} is small if compared to that normally used in other experiments ($400 - 1000MHz$) which is to say that the probability of populating the $6p$ level during the

excitation phase increases, given its $\frac{1}{\delta_{Blue}^2}$ dependence (given by the Bloch optical equation). The population of the intermediate state is not desirable because it can alter the dynamics and cause electric fields due to $6p$ atoms which are ionized after the absorption of another 421 photon. This poses a limitations on the maximum Ω_{Ryd} that can be used. Infact the transition $5s \rightarrow 70s$ is well described solely by a two-photon process when $\delta_{Blue} \gg \Omega_{Ryd}$, and in that case we can still neglet the population of the intermediate state. We lower Ω_{Ryd} acting on Ω_{421} because we want the $1012nm$ laser to have available the maximum power in the second part of the experiment. We furthermore verify with a detection performed $1\mu s$ after an excitation in absence of the $1012nm$ laser that the mean number of ions due to double-absorptions is less than 0.1.

After the excitation part, the experiment proceeds as follows.
The $421nm$ laser is switched off and simultaneously the RF of the $1012nm$ laser is switched, starting the de-excitation. After the $1012nm$ laser is switched off too we wait $30\mu s$ (as explained in the chapter on the experimental apparatus) and then perform the detection of the atoms which are still in the Rydberg state.

6.3 van der Waals spectroscopy

We want to use de-excitation to infer information about the distribution of energies of the Rydberg atoms in a certain spatial configuration.

From the interacting master equation we see that for small times the probability of de-excitation of the k atom is proportional to $\Gamma_k = \Gamma_0 \frac{1}{1+(\frac{1}{\gamma}(\delta - V_k))^2}$ (basically we consider only the states directly coupled to $\mu(0)$ i.e. the ones that differ from it by a single de-excitation). We expect that the probability of de-excitation with a certain detuning δ will be proportional to the number of atoms that have interaction energy close to δ within a width determined by the linewidth γ.

Then repeating the procedure with the same initial excitation scheme and varying the frequency of the de-excitation we can reconstruct the distribution of the energies of the initial configuration. The underlying idea is that this procedure can give us information about the spatial configuration of the excitations (figure 6.2).

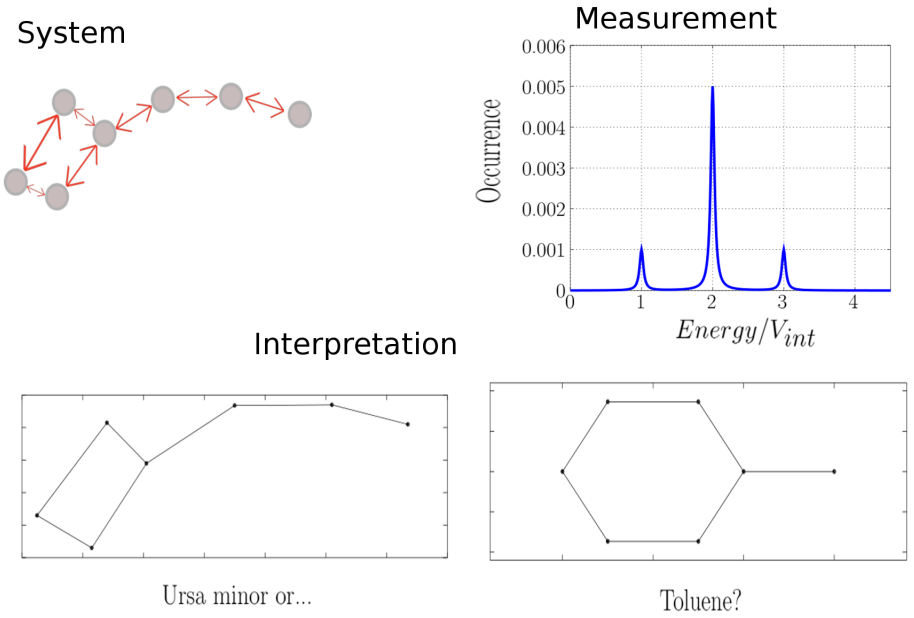

FIGURE 6.2: **Actual system, Measurement and interpretation of the results.** In the Ursa-minor configuration, the energy of each atom is given by the number of nearest neighbours: five atoms have two nearest neighbours and have $V_k = 2V_{int}$; only one atom has 3(1) nearest neighbours and has energy $V_k = 3V_{int}(1V_{int})$. Therefore if we choose $\delta = 2V_{int}$ we will de-excite an atom with a probability five times higher than if we choose $\delta = 3V_{int}$ or $\delta = V_{int}$. Note that energy distribution does not imply with certainty a spatial distribution.

At higher de-excitation times distortion of the observed spectrum may set in because of the growth of the non-linear terms in the exponential decay and also because de-excitation itself is a process which alters the interactions by removing Rydberg atoms: ideally, the spectrum of a determined configuration is reconstructed with the maximum accuracy when the probability of de-excitation of an atom is much less than 1 for every δ and with an average over a large amount of repetitions. Given the fluctuations of the system and of the experimental apparatus this limit is far from being satisfied: we are forced to choose a de-excitation time that is a compromise between accuracy and visibility. We also recall the fact that we can't produce deterministically the same initial state, the spectrum we are measuring must be intended as the average spectrum generated by that particular excitation scheme.

6.3.1 De-excitation after a resonant excitation

As we have seen in the introductory chapter the initial phase of the dynamics on resonance is dominated by excitations which appear randomly in the interaction volume at distances between them greater than R_b; after all the available blockade spheres are occupied there is a sudden slowing of the dynamics that implies that the new excitations

are produced with a decreased rate due to the interactions. We define N_c the number of excitations for which this sharp change of the slope happens. It can be estimated with the ratio between the interaction volume and the volume of a blockade sphere multiplied by the detection efficiency. We recall the fact that all the mean numbers the we are reporting refer to the measured mean number.

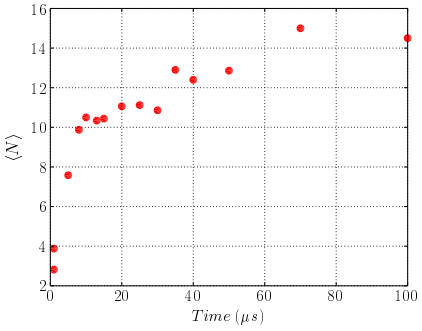

FIGURE 6.3: **Number of excitations as a function of the excitation time.** We can estimate that the change in slope around $N_c = 10$ signales the crossover between non-interacting and interacting excitations due to the saturation of the interaction volume by blockade spheres. 1D configuration, $\sigma_x = 181\mu m$, $\sigma_y = 27.6\mu m$

We first investigate de-excitation in the simplest case possible: we perform an excitation on resonance with a mean number of excitations (chosen varying the excitation time) that guarantees us that they are not interacting. We measure the number of atoms that remain in the Rydberg level (the ones that have not been de-excited) as a function of the de-excitation frequency

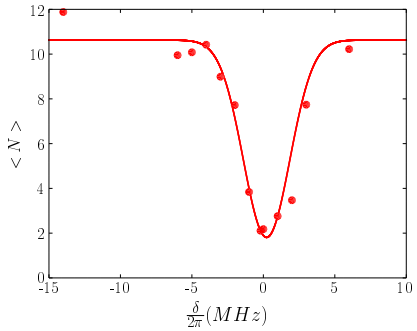

FIGURE 6.4: **De-excitation after a resonant excitation as a function of the de-excitation frequency.** 3D configuration. $\delta_{exc} = 0$, $\sigma_x = 160\mu m$, $\sigma_y = 93\mu m$.

The zero of the frequency axis is deduced from the relation $\delta_{Ryd} = \delta_{Blue} + \delta_{1012nm}$. It has an uncertainty $\sim \gamma$, beacuse that's the uncertainty with which we know δ_{Blue}.

We fit the curve with a lorentzian beacuse this is the behaviour expected if we look to the definition of the rates Γ_k (equation 6.5).

Figure 6.4 confirms that our picture of the excitation on resonance is correct: we can say that the atoms are not interacting because they are resonant with a $\delta = 0$ transition. We see that the linewidth γ is compatible with the expectations, with an extra consideration. Infact the measured linewidth is $\frac{\gamma_{meas}}{2\pi} = 2.6MHz$ against an expectation of $\frac{\gamma}{2\pi} = 1.3MHz$. As we have explained earlier, there is a distortion due to the non-small de-excitation time that in this case tends to broaden the measured linewidth.

We find that the offset of the lorentzian curve corresponds to the mean number of the excitation process.

Now we want to see what happens when we perform frequency scans starting from different initial numbers of the excitation on resonance, in particular when we reach the interacting regime. We change the initial condition simply by changing the excitation time.

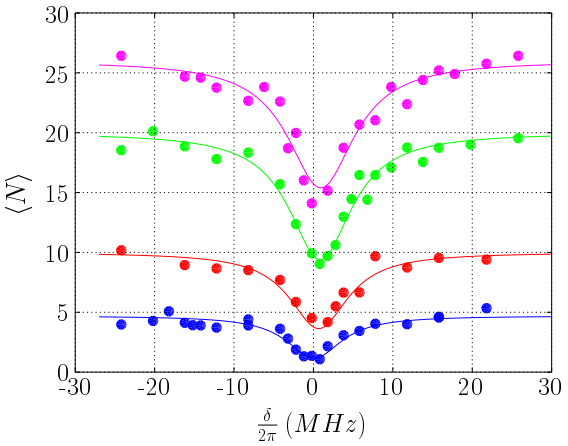

FIGURE 6.5: **De-excitation as a function of the detuning for different numbers of excitations created on resonance.** 1D configuration, $N_c = 15$. Initial numbers are 5 (blue), 10 (red),19(green) and 28 (purple). There is a small broadening of the resonance peak and a small shift towards higher energies as the initial number increases but the effect is clearly visible only analizing the lorentzian fit parameters.

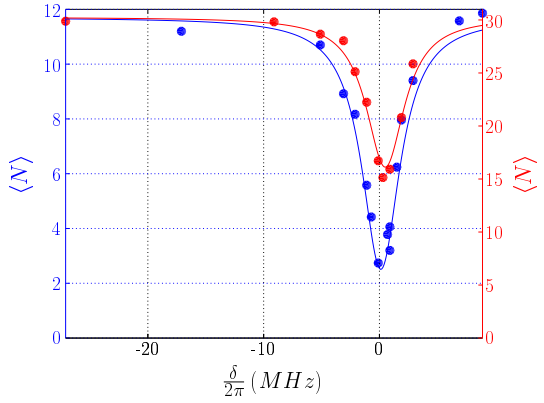

FIGURE 6.6: **De-excitation as a function of the detuning for two different numbers of excitations created on resonance** 3D configuration, $N_c \sim 20$. Initial number is 13 (Blue curve) and 30 (Red curve). With a higher number of initial excitations the de-excitation efficiency is lower because a fraction of atoms has non-zero energy.

We analyze the frequency scans with lorentzian fits. Even though a lorentzian model, which is symmetric, may seem too simple to take into account interactions, which can have influence only on the positive side of the spectrum, the examination of the parameters of the fits gives important information on the interactions.

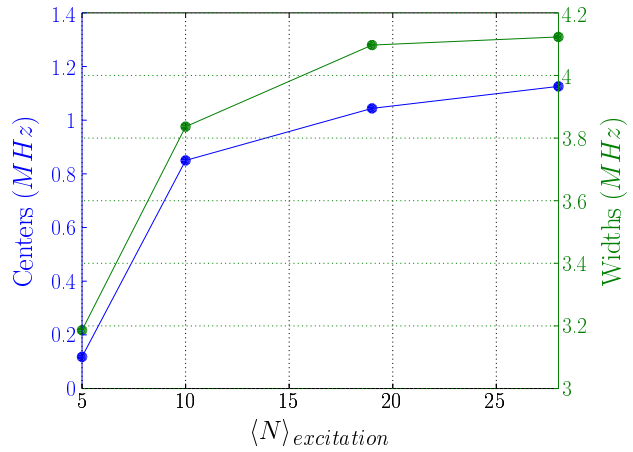

FIGURE 6.7: **Variation of the parameters of the lorentzian fits of the de-excitation frequency scans as a function of the number of excitations on resonance** The parameters of the lorentzian fits of the curves of fig. 6.5. As the number of initial excitations increases, there is a shift towards higher energies and a broadening of the de-excitation resonance peak. Both effects are of entity smaller than γ.

We found at first that the center of the lorentzian fits shifts towards higher energies as we increase the initial number while the width increases; these are a first sign of the interactions.

Both these effects are of entity smaller than γ, so they are marked by great relative error.

They are nevertheless confirmed by the simulations performed including both the excitation and de-excitation dynamics for a 1D chain of atoms at distance $\frac{R_b}{30}$ (figure 6.8).

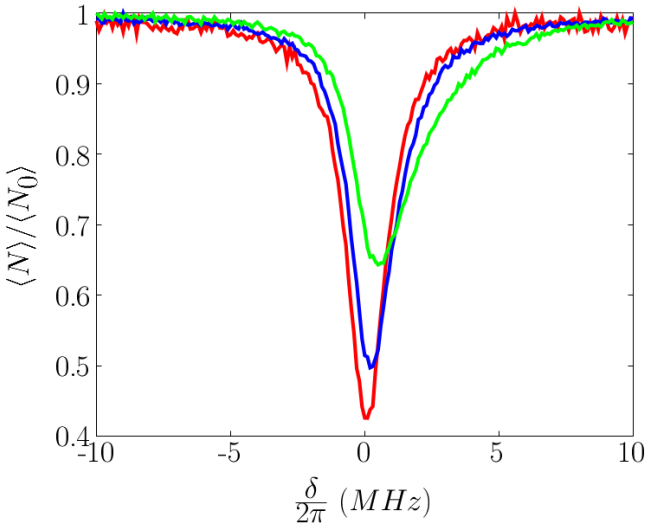

FIGURE 6.8: **1D de-excitation simulation of different initial numbers of Rydberg atoms created on resonance.** The curves are normalized to the initial numbers which are 9 (red curve), 20 (blue curve), 24 (green curve). There is a qualitative agreement with the experimental results: as the initial number of excitations increases, the efficiency of the de-excitation decreases due to the greater fraction of interacting atoms.

The most noticeable result is related to the efficiency of the de-excitation (the ratio between the fraction of atoms de-excited and the initial mean number) which decrease sensibly with higher initial numbers. We can see it more clearly in fig. 6.6.

This result is confirmed too by simulations which show also that as we increase the initial number occurrence of higher energies start to happen, but they are spread over a range much greater than γ.

In the experiment we can not reconstruct with accuracy the tail of the distribution because de-excitation involves a number of atoms smaller than the amount of fluctuations.

Then this implies that the excitations can be subdivided into two populations, one corresponding to the non-interacting atoms that can be de-excited on resonance and one corresponding to the interacting atoms which have energies spread along a range much greater than γ. The ratio between the number of interacting and the non-interacting ones increases as the initial number of excitations increases.

6.3.2 De-excitation after an off-resonant excitation

Now we want to see what changes when studying de-excitation of Rydberg atoms created with an excitation out of resonance. In this case we use only the 1D geometry beacuse of the simpler expected values for the interaction potential V_k. Infact in a 1D geometry each excitation can have, in a first approximation, only three de-excitation energies, which correspond to the situations of none, one or two neighbours at distance r_{fac}, with energies respectively 0, δ_{exc}, $2\delta_{exc}$ (with δ_{exc} being the detuning of the excitation frequency).

Next-nearest neighbours contribution can be neglected because they would be 2^6 times smaller. This would mean that the interaction spectrum of a perfect chain would have maximum occurrence of atoms at energy $2\delta_{exc}$ and only two atoms at δ_{exc}. Note that when we refer to an atom's energy we are referring to the interaction energy that it is sharing with the others near to it and that is necessary to add to the detuning in order to de-excite it. The total interaction energy is in fact $E = \frac{1}{2}\Sigma_k V_k$.

We perform excitations without seed with $\frac{\delta_{exc}}{2\pi} \sim 10 - 30MHz$. Since we know that atomic motion due to the finite temperature and to the van der Waals force can change the interaction energy we keep the total time of the excitation plus de-excitation phase $\sim 1\mu s$ which is near the lower limit of our apparatus in terms of time needed for completing such a sequence.

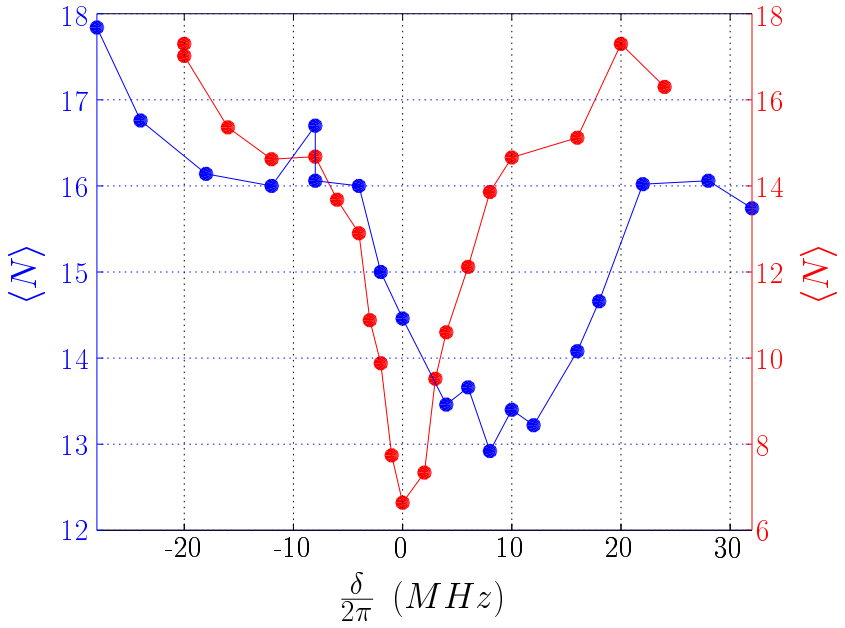

FIGURE 6.9: **De-excitation after an off-resonant excitation.** $\delta_{exc} = 10MHz$ (Blue points). The interactions shift the resonance curve by a factor close to δ_{exc}. For comparison, a curve of de-excitation after a resonant excitation of equal mean number is reported (Red Points).

If we compare the spectrum obtained with an excitation out of resonance with one obtained with an excitation on resonance of similar initial mean number we find a single broader peak shifted by $\sim \delta_{exc}$ (figure 6.9).

The fact that there are no other peaks at resonance or at $\delta = 2\delta_{exc}$, according to our previous reasoning, would lead us to the conclusion that we are dealing with couples of atoms at r_{fac}, without non-interacting seeds or long chains.

We will discuss this conclusion with the results of the next section.

The broadening of the peak is probabaly due to the motion of the atoms, as we have hipotized. A simple estimation of this effect which considers only the thermal motion (which is dominant at these detunings [6]) is the shift undergone by an excited atom which moves at thermal speed $v_{th} \sim 0.2\mu m/\mu s$ towards another excited atom at distance $r_{fac}(\delta = 30MHz)$. If the time of the experiment is $\tau = 1\mu s$ its final energy shift would be $\sim 6\frac{\delta_{exc}}{r_{fac}} v_{th}\tau = 9MHz$.

If we add a waiting time between the excitation and the de-excitation phase what we expect is an expansion of the Rydberg aggregate, to which both the thermal motion and the vdW repulsion concur, and a resulting decrease of the interaction energy due to the increased distances between particles.

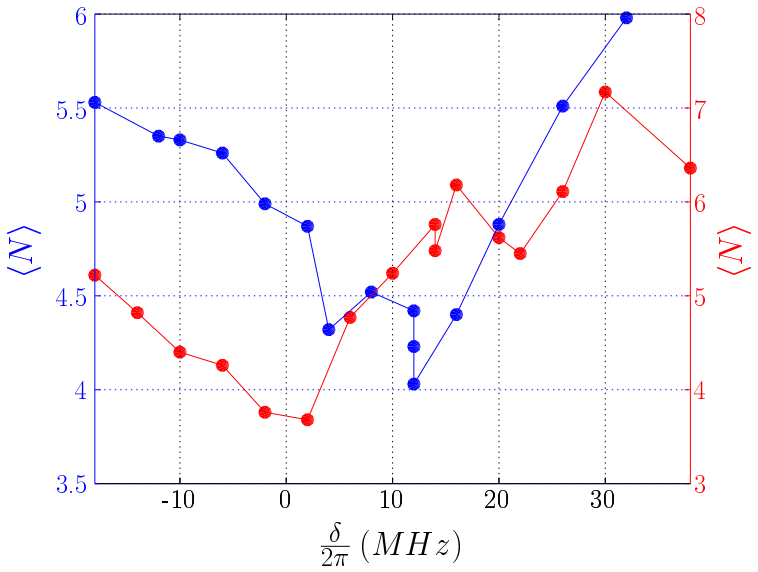

FIGURE 6.10: **Rydberg atoms expansion between an off-resonant excitation and the de-excitation.** Waiting time between excitation and de-excitation is $0.5\mu s$ (Blue points) and $10\mu s$ (Red points). During the waiting time the Rydberg aggregate expands due to thermal motion and vdW repulsion and its interaction energy decreases. $\delta_{exc} = 9MHz$

We see that, in this case, the spectrum is shifted towards lower energies (figure. 6.10). This proves that de-excitation is an extremely versatile technique, because it would allow also to record the time evolution of the interaction energies due to the atomic motion.

6.4 A new dynamics

As we have already evidenced, de-excitation is a destructive measure of the interaction spectrum: when an atom is brought to the ground state, the potential felt by the others changes. We want to see how this dynamics evolves to find trace of these correlations. Again we make use of 1D simulations.

The experiment is performed as before, we simply change the de-excitation time while keeping fixed the laser frequency on resonance with the de-excitation transition that we determine with a frequency scan.

6.4.1 De-excitation dynamics after an excitation on resonance

As before, we verify the simplest case first: we excite atoms on resonance in a number which guarantees us that they are not interacting and we measure the number of atoms

that remain after a variable de-excitation time on resonance with the de-excitation transition ($\delta = 0$).

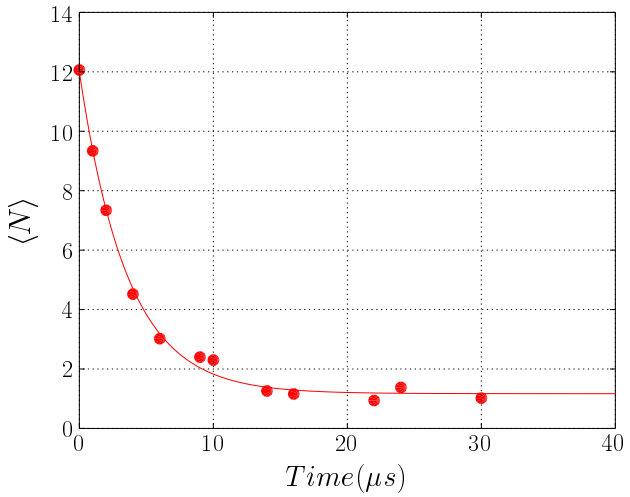

FIGURE 6.11: **De-excitation as a function of the de-excitation time** As predicted by the theory, in absence of interactions, de-excitation is exponential.

As expected, the decay is well fitted by an exponential curve. The offset is due to the black body radiation-induced transfer to other Rydberg states which are measured because of our non-selective detection. The decay rate is smaller by a factor $\sim 4-10$ than the value of Γ estimated knowing the power of the laser, the $6p$ lifetime, the laser waist and the dipole matrix elements and evaluating the gaussian beam power profile at the peak. Then a non-perfect alignment can easily produce such a discrepancy.

Again, as before, we repeat the same experiment starting from different initial numbers created on resonance and in particular in the interacting regime.

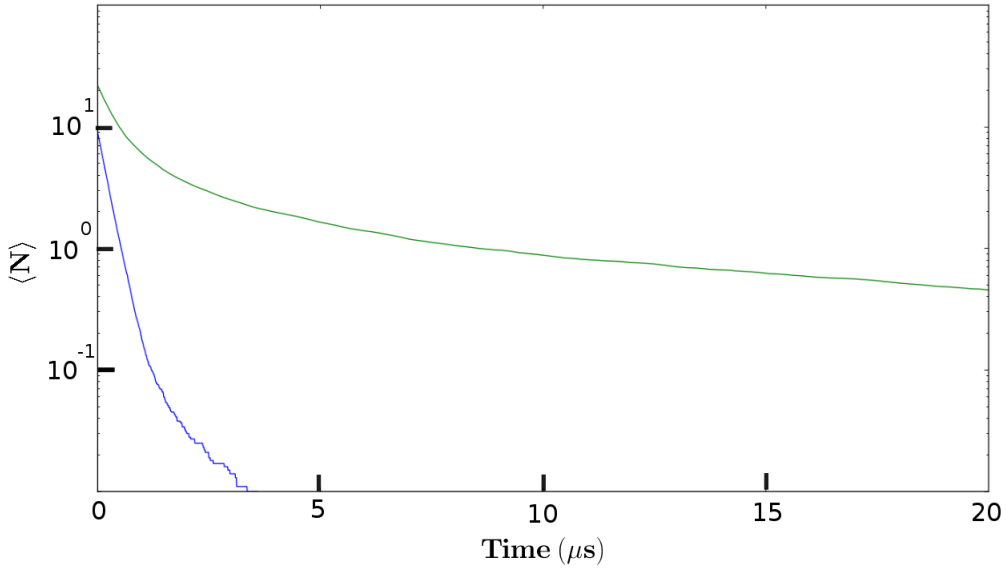

FIGURE 6.12: **Simulation of de-excitation as a function of de-excitation time of interacting excitations** At higher initial numbers we expect that the atoms that start interacting have a slower de-excitation rate and infact the final rate of the curve at higher initial number is lower than the rate of the curve that starts from a lower initial number.

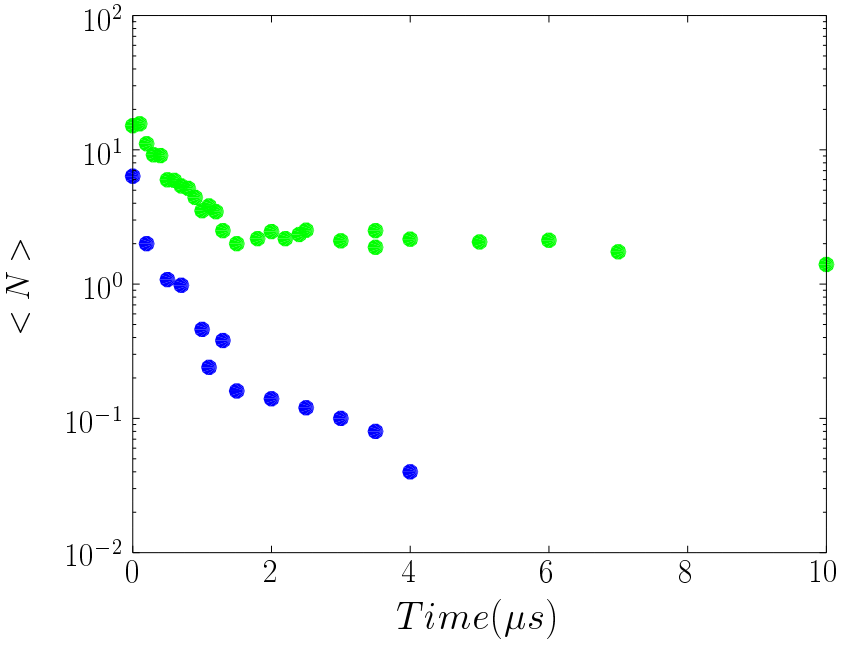

FIGURE 6.13: **De-excitation as a function of de-excitation time of interacting excitations** 1D configuration. The green curve which starts from a higher initial number (15.6) has a sharp slope change at the crossover between the fast de-excitation of non-interacting atoms and the slow de-excitation of interacting atoms. The blue curve has an initial number of excitations of 6, and has an almost constant de-excitation rate.

What we see (fig. 6.13), and it is confirmed by simulations (see fig. 6.12), is that $\langle N \rangle$ seems to decay with a faster rate in the first part of the dynamics, and with a slower one in the second. We use semilogarithmic graphs in order to give similar weights to the two regimes and to evidence the deviation from a linear curve that we would see in the case of a perfecly exponential decay; we want to stress though that to associate the slope of the curve in a certain point to an actual rate would be improper because we are observing an average over different rates of different energy classes. We associate these two part of the dynamics with the de-excitation respectively of the non-interacting atoms, which are rapidly de-excited, and of the interacting ones that feel a smaller Γ due to the interactions. This subdivision into two populations of the atoms has already been seen in the spectroscopy of resonant excitations: as the initial number is increased, an increasing fraction of atoms ends in the tail of the distribution.

This can be more clearly seen in a simulation of de-excitation starting from an almost ordered state. The initial configuration is a 1D configuration of N_0 excitations spaced by a distance a plus $n < N_0$ random excitations between, at a distance $\frac{a}{2}$ from the neighbours.

a is such that: $V_{int}(r, r \pm a) < \gamma$, $V_{int}(r, r \pm \frac{1}{2}a) > \gamma$ so that the atoms in the regular chain do not interact with each other, while the random excitations and their neighbours interact. The simulated de-excitation dynamics from such states show that the dynamics slows when $\langle N \rangle \sim 3n$ which confirms our interpretation.

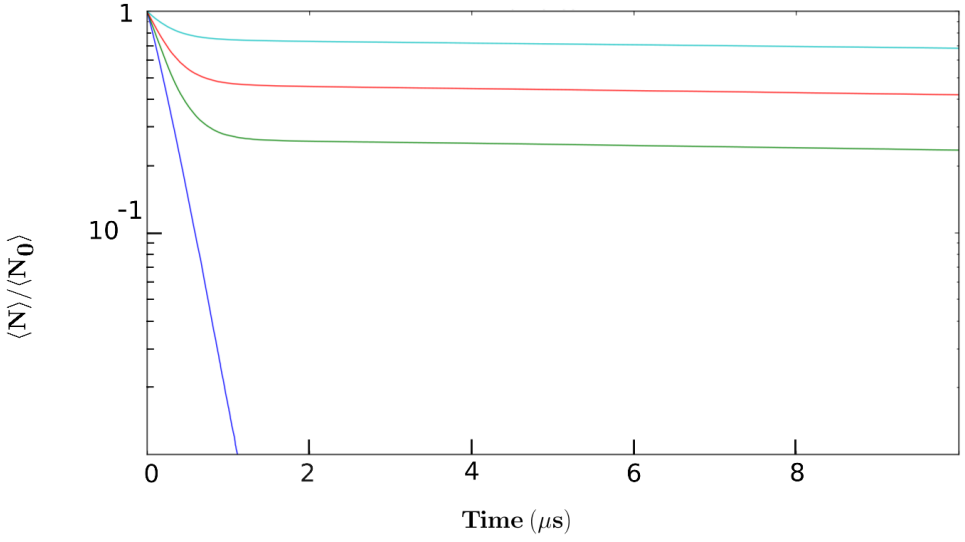

FIGURE 6.14: **Simulation of de-excitation of ordered states.** The initial state is a chain of N Rydberg atoms with n Rydberg atoms in random positions between them as a function of the de-excitation time. $N_0 = 100, n = 0(blue), n = 5(green), n = 10(red), n = 20(lightblue)$. The number of atoms that are slowly de-excited is the number of interacting atoms due to the intersitial excitations.

These results show that the experimental $\langle N \rangle$ where the change of slope occours can be used as a measure of the numbers of the interacting atoms in the initial configuration (and by difference, of the number of non-interacting atoms).

Moreover, this imply that at that particular time of the de-excitation dynamics we have created a state formed, with high probability, by interacting excitations.

The two-populations interpretation becomes too simplistic when the excitation is performed with the 3D geometry, where each excitation has multiple interaction possibilities, in terms of spatial degrees of freedom and number of nearest neighbours.

In this case we do not see a sharp but rather a continuos change of the slope of the mean number of atoms which remain in the Rydberg level as a function of the de-excitation time.

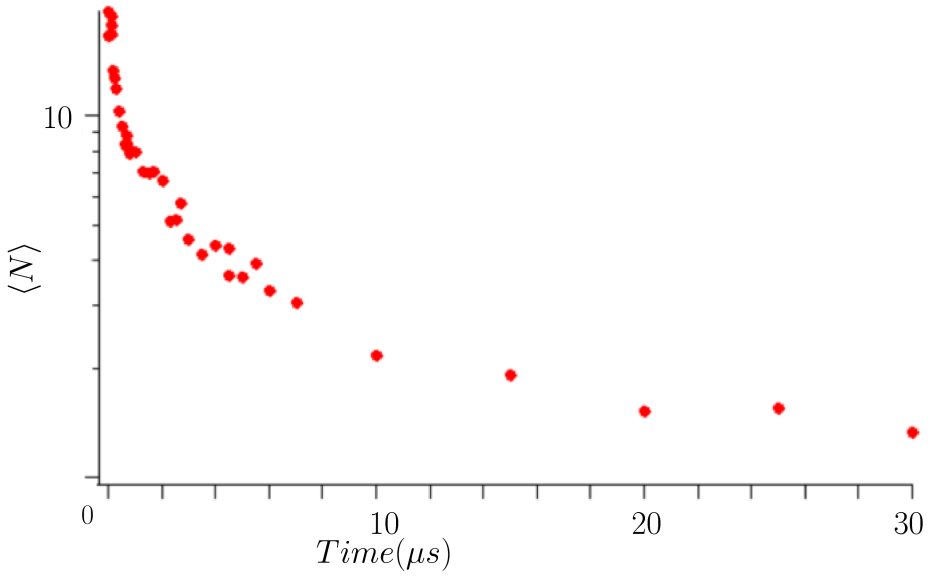

FIGURE 6.15: **De-excitation after a resonant excitation as a function of the de-excitation time in a 3D geometry.** The 3D geometry offers multiple possibilities of interactions and hence eliminates the sharp division between interacting and non-interacting atoms, so there is a continuos change of the apparent de-excitation rate.

These results lead us to some considerations about the validity of mean field approximations for this kind of systems. Infact the dynamics of Rydberg excitation is often integrated numerically by replacing the interaction strength of the k atom, V_k, with an average interaction strength (as can be found in [9]). We have found instead that the distribution of the interaction strengths can have large fluctuations around the mean value, both in the case where we have two atomic populations at zero and non-zero energy (1D case) and in the case where more interaction possibilities are present (3D case).

6.4.2 De-excitation dynamics out of resonance

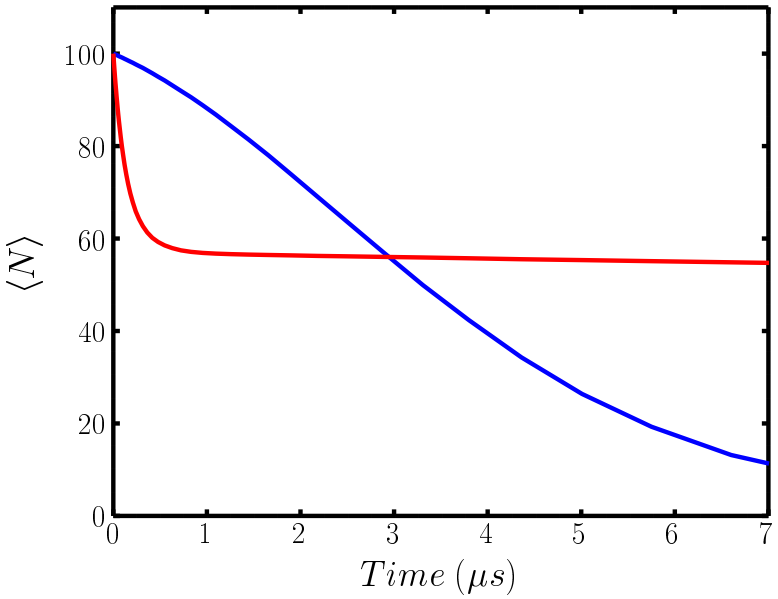

FIGURE 6.16: **Simulation of a detuned de-excitation of an ordered chain.** The excitations are initially spaced by $r_{fac}(30MHz)$. De-excitation is performed with $\frac{\delta}{2\pi} = 15MHz$ (Blue curve) and $\frac{\delta}{2\pi} = 30MHz$ (Red curve). The first de-excitation stops when no atoms have two nearest neighbours, the second has always the possibility of resonant de-excitation at the ends of the chain

We have not yet realized an experiment in this context. The main difficulty is the fact that we can't locate a precise resonance at $2\delta_{exc}$, which is to say that de-excitation is extremely non-efficient in this regime. In light of the simulation of fig. 6.16 we can see that after a certain point the de-excitation with $\delta = \delta_{exc}$ becomes faster while the other (at $\delta = 2\delta_{exc}$) is blocked. This can be geometrycally explained by seeing that the de-excitation at $\delta = 2\delta_{exc}$ concerns only atoms with two nearest neighbours excited, and it blocks when the chain has holes separated by an atom or at least two, therefore the fast de-excitation of a chain concerns only $33 - 50\%$ of the initial number. Instead, a de-excitation at $\delta = \delta_{exc}$, after the de-excitation of the first atom, is again resonant with the new head of the chain and ideally it stops only when there is only one atom left.

The experimental fluctuations may shorten even more this initial regime where the $\delta = 2\delta_{exc}$ de-excitation is more efficient and that could be the explanation of the absence of the peak at $\delta = 2\delta_{exc}$ (figure 6.9).

6.5 Conclusions

Here we have just demonstrated some of the many possibilities that de-excitations offers in the context of interacting Rydberg atoms, even though it could be generalized to any system composed by two-level elements that interact with each other that can be brought into a non-interacting state.

We provided a new method to assess the distribution of the interaction energy between Rydberg atoms, and we have shown how this can be used to gain information also on their spatial configuration. We have also have highligthed what are the intrinsic limitations of this procedure.

Moreover, we have shown that de-excitation dynamics is a highly-correlated process just as excitation dynamics and therefore allows a specular point of view on the same complex, many-body problem.

We have shown how de-excitation dynamics too gives information about the initial state in terms of energy and space, but we also introduced the possibility to use it as a way to manipulate the system itself by removing selectively a class of atoms that have a particular energy.

Chapter 7

Conclusions

In this thesis we have tried to investigate the dynamics of a complex many body system with the aid of a dissipative dynamics. In particular, this study was applied to the laser-driven excitation dynamics of a cold cloud of interacting Rydberg atoms and the dissipative dynamics was provided by a coupling with a fast-decaying level, hence the term de-excitation dynamics.

We have found that de-excitation can reveal a lot of information about a system prepared with the excitation dynamics; this information is related to the interactions between Rydberg atoms and their spatial arrangement. Also, this extra information was gained without the need for additional observables such as the positions of the excitations.

The work presented here only touches the surface of what can be done using de-excitation as a tool in cold Rydberg atom physics. Other experiments are needed to answer the questions that have remained open, and to explore the possibilities offered by the de-excitation applied to other aspects of strongly correlated Rydberg excitations.

The general scheme of the de-excitation, however, can be extended to any system of interacting elements that can be coupled to a fast-decaying level, as we have mentioned.

We suggest that it could be used also in a quantum simulation perspective [8], i.e. to simulate a dissipative dynamics with the advantage that the dissipation rate can be easily tuned acting on the strength of the coupling with the fast-decaying level.

We conclude with a final remark on the idea we presented in the preface.

We think that that the success of de-excitation as a tool for gaining information about the excitation dynamics is due to the fact that the dynamics it induces is simpler: by this we mean that has fewer degrees of freedom, and that it is described by simpler equations. We hope that this concept could be generalized and will find applications

also in different contexts of many-body physics.
$|end\rangle$

Bibliography

[1] P. W. Anderson. More Is Different. *Science (80-.).*, 177(4047):393–396, 1972.

[2] Daniel Comparat and Pierre Pillet. Dipole blockade in a cold Rydberg atomic sample. 2010.

[3] A. Dauphin, M. Müller, and M. A. Martin-Delgado. Rydberg-atom quantum simulation and Chern-number characterization of a topological Mott insulator. *Physical Review A*, 86(5):053618, 2012.

[4] Y. O. Dudin, L. Li, F. Bariani, and A. Kuzmich. Observation of coherent many-body Rabi oscillations. *Nature Physics*, 8:790–794, 2012.

[5] Matthew Ebert, Alexander Gill, Michael Gibbons, Xianli Zhang, Mark Saffman, and Thad G. Walker. Atomic fock state preparation using rydberg blockade. *Phys. Rev. Lett.*, 112:043602, 2014.

[6] R. Faoro, C. Simonelli, M. Archimi, G. Masella, M. M. Valado, E. Arimondo, R. Mannella, D. Ciampini, and O. Morsch. Van der Waals explosion of cold Rydberg clusters. *ArXiv e-prints*, 2015.

[7] Thomas F. Gallagher. *Rydberg Atoms*. Cambridge University Press, 2005.

[8] I. M. Georgescu, S. Ashhab, and F. Nori. Quantum simulation. *Reviews of Modern Physics*, 86:153–185, 2014.

[9] Igor Lesanovsky and Juan P. Garrahan. Kinetic constraints, hierarchical relaxation, and onset of glassiness in strongly interacting and dissipative rydberg gases. *Phys. Rev. Lett.*, 111:215305, 2013.

[10] N. Malossi, M. M. Valado, S. Scotto, P. Huillery, P. Pillet, D. Ciampini, E. Arimondo, and O. Morsch. Full Counting Statistics and Phase Diagram of a Dissipative Rydberg Gas. *Physical Review Letters*, 113(2):023006, 2014.

[11] L. Mandel. Squeezed States and Sub-Poissonian Photon Statistics. *Phys. Rev. Lett.*, 49(2):136–138, 1982.

[12] H. J. Metcalf and van der Straten. *Laser cooling and trapping.* Springer, 1999.

[13] I. Mourachko, D. Comparat, F. de Tomasi, A. Fioretti, P. Nosbaum, V. M. Akulin, and P. Pillet. Many-body effects in a frozen rydberg gas. *Phys. Rev. Lett.*, 80:253–256, 1998.

[14] Marcel Mudrich, Nassim Zahzam, Thibault Vogt, Daniel Comparat, and Pierre Pillet. Back and forth transfer and coherent coupling in a cold rydberg dipole gas. *Phys. Rev. Lett.*, 95:233002, 2005.

[15] P. Schauß, J. Zeiher, T. Fukuhara, S. Hild, M. Cheneau, T. Macrì, T. Pohl, I. Bloch, and C. Gross. Crystallization in ising quantum magnets. *Science*, 347(6229):1455–1458, 2015.

[16] C. Simonelli, M. Martinez Valado, G. Masella, L. Asteria, E. Arimondo, D. Ciampini, and O. Morsch. Seeded excitation avalanches in off-resonantly driven Rydberg gases. *ArXiv e-prints*, 2016.

[17] Cristiano Simonelli. *Studi sperimentali di eccitazioni di stati di Rydberg fortemente correlate in gas ultrafreddi.* Master thesis, Università degli Studi di Pisa, 2014.

[18] R M W van Bijnen, S Smit, K A H van Leeuwen, E J D Vredenbregt, and S J J M F Kokkelmans. Adiabatic formation of rydberg crystals with chirped laser pulses. *Journal of Physics B: Atomic, Molecular and Optical Physics*, 44(18):184008, 2011.

[19] M. Viteau, P. Huillery, M. G. Bason, N. Malossi, D. Ciampini, O. Morsch, E. Arimondo, D. Comparat, and P. Pillet. Cooperative Excitation and Many-Body Interactions in a Cold Rydberg Gas. *Physical Review Letters*, 109(5):053002, 2012.